

Department of Physics and Astronomy

University of Heidelberg

Master thesis

in Physics

submitted by

Lukas Witola

born in Bonn

2019



**Calibration and performance studies of the readout**

**ASIC for the LHCb SciFi Tracker**

This Master thesis has been carried out by Lukas Witola

at the

Physikalisches Institut Heidelberg

under the supervision of

Herrn Prof. Ulrich Uwer



## **Abstract**

The LHCb experiment will perform a major upgrade of the detector during the LHC's Long Shutdown 2 from 2019 to 2020. The upgrade will enable the detector to operate at an increased instantaneous luminosity and to record data at the LHC bunch crossing rate of 40 MHz. The new operating conditions require the replacement of the complete tracking system. The tracking stations downstream of the magnet will be replaced by the SciFi Tracker, a large, high granular scintillating fibre tracker, readout by arrays of silicon photomultipliers (SiPMs). The signals are processed by a custom 64-channel ASIC called PACIFIC. Each channel implements an analogue processing chain and three comparators with adjustable thresholds for digitisation. The comparator thresholds need to be calibrated with respect to the connected SiPM channel to ensure a high performance of the detector. A calibration method, based on an analytical description of the SiPM pulse height spectrum, has been investigated and several factors that impair the calibration have been identified.

The performance of a full detector slice of the SciFi Tracker regarding the hit efficiency, hit resolution, and spillover has been studied on data obtained during a test beam campaign at the CERN SPS in July 2018.

## **Kurzfassung**

Das LHCb Experiment führt während des LHC Long Shutdown 2 in den Jahren 2019 bis 2020 ein umfassendes Upgrade des Detektors aus. Der Detektor wird dadurch in der Lage sein bei einer erhöhten Luminosität und mit einer Rate von 40 MHz, entsprechend der Kollisionsrate am LHC, Daten zu nehmen. Um unter den neuen Bedingungen weiterhin präzise Ergebnisse zu liefern, werden sämtliche Spurkammern ersetzt. Die Hauptspurkammern hinter dem Magneten werden durch den SciFi Tracker ersetzt, dessen Hauptkomponenten szintillierende Fasern und Silizium-Photomultiplier (SiPMs) sind. Die Signale werden vom PACIFIC Chip weiterverarbeitet und mit Hilfe von drei Komparatoren digitalisiert.

Die Schwellen der Komparatoren müssen in Bezug auf den angeschlossenen SiPM Kanal kalibriert werden. Hierzu wurde eine Methode basierend auf einer analytischen Beschreibung des SiPM Pulshöhenspektrums untersucht und mehrere Faktoren identifiziert, welche die Kalibrierung beeinträchtigen.

Im Weiteren wurden die Detektionseffizienz, Ortsauflösung, sowie Spillover-Effekte des vollständigen Detektosystems anhand von Daten, welche während einer Testkampagne am CERN SPS im Juli 2018 genommen wurden, vermessen.



# Contents

|          |   |           |
|----------|---|-----------|
| <b>1</b> | <b>Introduction</b>                               | <b>1</b>  |
| <b>2</b> | <b>Physics at the LHC</b>                         | <b>3</b>  |
| 2.1      | The Standard Model of particle physics . . . . .  | 3         |
| 2.2      | The weak interaction of quarks . . . . .          | 4         |
| <b>3</b> | <b>The LHCb experiment and its upgrade</b>        | <b>7</b>  |
| 3.1      | The LHCb detector . . . . .                       | 7         |
| 3.1.1    | Tracking . . . . .                                | 8         |
| 3.1.2    | Particle identification . . . . .                 | 12        |
| 3.2      | The LHCb detector upgrade . . . . .               | 14        |
| <b>4</b> | <b>The LHCb SciFi Tracker</b>                     | <b>17</b> |
| 4.1      | Requirements . . . . .                            | 17        |
| 4.2      | Layout of the LHCb SciFi Tracker . . . . .        | 18        |
| 4.3      | Working principle . . . . .                       | 18        |
| 4.4      | Scintillating fibres . . . . .                    | 19        |
| 4.5      | Fibre mats and modules . . . . .                  | 20        |
| 4.6      | Silicon photomultipliers . . . . .                | 21        |
| 4.6.1    | Working principle . . . . .                       | 21        |
| 4.6.2    | SiPM characteristics . . . . .                    | 22        |
| 4.6.3    | Pulse shape . . . . .                             | 24        |
| 4.6.4    | SiPM pulse height spectrum . . . . .              | 26        |
| 4.7      | Frontend electronics . . . . .                    | 27        |
| 4.8      | Light injection system . . . . .                  | 28        |
| 4.9      | Hit reconstruction . . . . .                      | 28        |
| <b>5</b> | <b>The PACIFIC ASIC</b>                           | <b>31</b> |
| 5.1      | Design . . . . .                                  | 31        |
| 5.2      | PACIFICr5q, the production version ASIC . . . . . | 33        |
| 5.2.1    | Improvement in signal spillover . . . . .         | 34        |
| 5.2.2    | Shaper settings . . . . .                         | 35        |
| <b>6</b> | <b>Calibration of the PACIFIC thresholds</b>      | <b>37</b> |
| 6.1      | Threshold scan . . . . .                          | 37        |
| 6.2      | Threshold determination . . . . .                 | 37        |
| 6.3      | Calibration quality . . . . .                     | 41        |
| 6.4      | Low calibration light intensity . . . . .         | 43        |

|          |  |           |
|----------|--|-----------|
| 6.5      | Increasing the light intensity . . . . . | 45        |
| <b>7</b> | <b>Performance of PACIFICr5q</b>         | <b>47</b> |
| 7.1      | Integrator response . . . . .            | 47        |
| 7.2      | Tracking performance . . . . .           | 49        |
| 7.2.1    | Hit efficiency . . . . .                 | 51        |
| 7.2.2    | Hit resolution . . . . .                 | 53        |
| 7.2.3    | Spillover probability . . . . .          | 53        |
| <b>8</b> | <b>Summary</b>                           | <b>57</b> |
|          | <b>Bibliography</b>                      | <b>62</b> |

# 1 Introduction

The Standard Model (SM) of particle physics [1–3], developed during the second half of the 20th century, is a theory with great success and is able to explain almost every experimental observation in the field of particle physics. It describes the properties and interactions of all elementary particles and has precisely predicted the existence of several phenomena that were observed subsequently. In 2012, the last missing fundamental particle of the SM, the Higgs boson [4, 5], was discovered at the Large Hadron Collider (LHC).

However, the SM is not a complete theory of all particles and forces, since gravity, albeit negligible at the subatomic scale, is not incorporated. Further observations that the theory is not able to describe include dark matter [6], the non-zero neutrino mass [7, 8], and the matter-antimatter asymmetry of the universe [9]. These observations demand new theories beyond the Standard Model, which are referred to as New Physics (NP).

The LHC, with its unprecedented centre-of-mass energy and luminosity<sup>1</sup>, provides a suitable environment for the search of NP phenomena. The LHCb experiment is located at one of the four interaction points of the LHC and is a dedicated experiment for high-precision measurements of processes involving heavy quarks<sup>2</sup>. During its first two data taking campaigns from 2010 until the end of 2018 the experiment recorded the world’s largest data sample of reconstructed processes involving heavy quarks [10]. This data enables precise measurements of the parameters of the SM and provides strong constraints for possible NP theories. The statistical sensitivity of many LHCb measurements has the potential to improve to levels similar, or even beyond the precision of SM calculations [11]. However, it is not possible to record the required amount of data with the current detector in a reasonable amount of time. It will be achieved by an upgrade of the detector that takes place from 2019 to 2020 during the LHC’s Long Shutdown 2 (LS 2).

The upgrade relies on two major changes. Firstly, the low level hardware trigger which preselects potentially interesting events and whose rate is currently limited to 1.1 MHz by the readout electronics of some subdetectors, will be removed and replaced by a software trigger operating at the LHC beam crossing rate of 40 MHz [12]. Secondly, the detector will be operated at a five times higher

---

<sup>1</sup>Luminosity ( $\mathcal{L}$ ) is a measure of the interaction rate at particle colliders and is defined as  $\mathcal{L} = \dot{N}/\sigma$ . With the reaction rate  $\dot{N}$  and the cross section  $\sigma$ , which is proportional to the probability that an interaction will occur.

<sup>2</sup>Quarks are one family of fundamental particles in the SM and are distinguished by their mass. The term heavy quarks in general refers to the charm and beauty quarks. More information on the structure of the SM and the physics of quarks is provided in Chap. 2.

luminosity [12]. These changes require the replacement of several subsystems. The tracking system after the bending magnet currently consists of two detectors: a silicon microstrip detector covering the region around the beam pipe, and a large straw drift tube detector covering the remaining area. It will be replaced by the SciFi Tracker, a detector based on scintillating fibres readout by silicon photomultipliers (SiPMs). The SiPM signals are processed by a chain of frontend electronics, which include the PACIFIC<sup>3</sup> readout chip. The PACIFIC is a custom 64-channel ASIC<sup>4</sup> designed for the readout of SiPMs with a sampling frequency of 40 MHz. Each channel of the ASIC is directly connected to one of the SiPM channels and implements an analogue processing chain which shapes, integrates, and digitises the SiPM pulses. The digitisation of the integrated signal is based on three comparators with adjustable thresholds.

The goal of this thesis is to provide a reliable method to calibrate the PACIFIC comparator thresholds with respect to the response of the connected SiPM channel and to validate the performance of prototypes of the SciFi Tracker with PACIFICr5q, the final version of the chip.

Chapter 2 gives an introduction to the physics studied at the LHC and in particular at LHCb. The following chapter (Chap. 3) provides an overview of the LHCb detector and its upgrade with a focus on the tracking system. The SciFi Tracker is explained in more detail in Chap. 4. Chapter 5 introduces the PACIFIC, starting with an explanation of its general design and functionality and finishing with a section dedicated to PACIFICr5q, where the distinctive change in the design and two sets of operational parameters are introduced. Chapter 6 describes a method to calibrate the PACIFIC comparator thresholds based on an analytical model of the SiPM pulse height spectrum and discusses several influences on the quality of the calibration. Studies of the performance of PACIFICr5q are presented in Chap. 7. The chip was first evaluated in lab measurements and then used in a test beam campaign, where the tracking performance of prototypes of the SciFi Tracker was studied. Key performance parameters are measured and compared to the detector requirements. An overall summary is given in Chap. 8.

---

<sup>3</sup>Low Power ASIC for the SCIntillating Fibre TraCker

<sup>4</sup>Application-specific integrated circuit

## 2 Physics at the LHC

The European Organisation for Nuclear Research (CERN), near Geneva, Switzerland, is one of the world's largest facilities for high energy physics. Its mission is to uncover the fundamental laws of our universe by studying the characteristics and interactions of elementary particles. For this, CERN provides a number of accelerators that deliver particle beams of different types, intensities and energies. The LHC, CERN's flagship, is the largest accelerator in the world, with a circumference of 27 km. It accelerates two proton beams in opposing directions up to 6.5 TeV each and collides them at four points where the main experiments ALICE, ATLAS, CMS and LHCb are located. Besides proton-proton collisions, the LHC also provides heavy ion-proton, and heavy ion-heavy ion collisions. The data recored by all four experiments allows for a wide physics program.

The aim of this chapter is to give an introduction to the physics that is being studied at the LHC and in particular at the LHCb experiment. It loosely follows the introduction given in Ref. [13].

### 2.1 The Standard Model of particle physics

The Standard Model of particle physics is currently the theory that best describes our understanding of the universe at the quantum level. It provides a description of three of the four known fundamental forces, the electromagnetic, weak and strong interactions, with gravity not included, and all known elementary particles.

The elementary particles described by the SM can be categorised in three distinct groups: fermions, gauge bosons, and the Higgs boson.

Fermions are spin one-half particles and the constituents of all visible matter. They are further classified based on the type of interactions they experience. All twelve of them interact via the weak force and with the exception of the three neutrinos, which are electrically neutral, also via the electromagnetic force. The nine quarks in addition also carry the strong interaction equivalent of the electric charge called colour charge. Due to the nature of the strong interaction, quarks are never observed as free particles, only in bound states of two or three quarks, called mesons and baryons, respectively. This property distinguishes the quarks from the leptons.

A peculiar feature of the SM is that both quarks and leptons appear in three so-called generations, where the second and third generation are essentially copies of the first one, differing only in their mass. The muon ( $\mu^-$ ), for example, is a heavier copy of the electron ( $e^-$ ), with  $m_\mu \approx 200m_e$ . The origin of this structure, if there is one, is currently not understood.

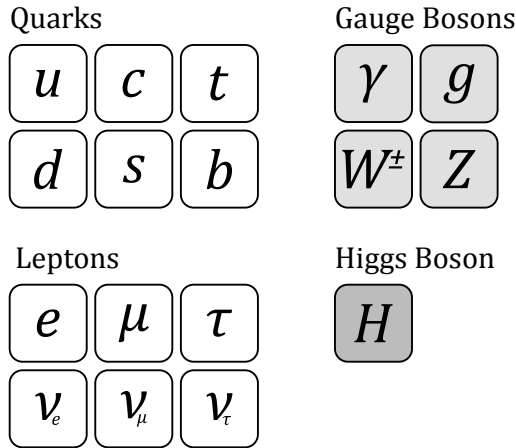


Figure 2.1: Fundamental particles of the Standard Model.

In the SM interactions between elementary particles are described in the framework of Quantum Field Theory [13, 14] where forces are mediated by the exchange of vector (spin=1) gauge bosons. In the case of the electromagnetic interaction the gauge boson is the familiar photon. The force-carrier of the strong interaction, which confines quarks into bound states, is called gluon. Both photons and gluons are massless, whereas the gauge bosons of the weak interaction are about 80 to 90 times more massive than a proton. The charged and neutral currents of the weak interaction are mediated by the charged  $W^+$  and  $W^-$ , and the neutral  $Z$ , respectively.

The Higgs boson is the only scalar (spin=0) elementary particle in the SM. It provides the mechanism by which all other fundamental particles acquire their mass [15, 16].

## 2.2 The weak interaction of quarks

Quarks are the only particles in the SM that carry fractional electric charge  $q$ , with  $q = +2/3e$  for the *up-type* quarks ( $u, c, t$ ) and  $q = -1/3e$  for the *down-type* quarks ( $d, s, b$ ). The nine different types of quarks are referred to as flavour.

The weak charged-current interaction, mediated by the charged  $W^+$  and  $W^-$  bosons, only couples together pairs of fundamental fermions that differ by one unit of the elementary charge  $e$ , in order to conserve charge. It is the only interaction that mediates transitions between two quark flavours, which becomes particular important considering particle decays. The relative coupling strength of these transitions is parametrised by the unitary<sup>1</sup> Cabibbo-Kobayashi-Maskawa (CKM) matrix. The

---

<sup>1</sup> $V^\dagger V = I$

transition of a  $d$  quark to  $d$ , for example, is associated with the matrix element  $V_{ud}$ .

$$V_{CKM} = \begin{pmatrix} V_{ud} & V_{us} & V_{ub} \\ V_{cd} & V_{cs} & V_{cb} \\ V_{td} & V_{ts} & V_{tb} \end{pmatrix} \quad (2.1)$$

The magnitude of the CKM matrix elements cannot be calculated within the SM and needs to be measured from interactions of mesons and baryons containing the respective quarks. The measured magnitudes are taken from Ref. [17] and summarised in Eq. 2.2. The diagonal elements are close to unity and the off-diagonal elements are consequently smaller, to ensure unitarity. The near diagonal form of the CKM matrix leads to the suppression of weak interactions between quarks of different generations, relative to those within the same generation. The suppression is largest for interaction between the first and third generation.

$$\begin{pmatrix} |V_{ud}| & |V_{us}| & |V_{ub}| \\ |V_{cd}| & |V_{cs}| & |V_{cb}| \\ |V_{td}| & |V_{ts}| & |V_{tb}| \end{pmatrix} = \begin{pmatrix} 0.975 & 0.225 & 0.004 \\ 0.224 & 0.974 & 0.042 \\ 0.009 & 0.041 & 0.999 \end{pmatrix} \quad (2.2)$$

Since the CKM matrix is a unitary  $3 \times 3$  matrix, it can be described by three rotation angles and one complex phase. In the SM this complex phase is non-zero and gives rise to the phenomenon of CP-violation which is a violation of the charge conjugation parity (CP) symmetry. CP-symmetry states that the laws of physics should be the same if a particle is exchanged with its antiparticle (C-symmetry) while inverting the spatial coordinates (P-symmetry). This symmetry implies that the process  $A \rightarrow X$  for particles  $A$  and  $X$  occurs with the same rate as the equivalent antiparticle process  $\bar{A} \rightarrow \bar{X}$ . In the presence of a complex phase however this symmetry is violated if the process  $A \rightarrow X$  involves two different transitions with a relative phase difference between them.



### 3 The LHCb experiment and its upgrade

The LHCb experiment is a dedicated experiment for precision measurements of  $CP$ -violation and rare decays of hadrons containing  $b$  and  $c$  quarks, *e.g.*  $B$  and  $D$  mesons. At the energies provided by the LHC  $b\bar{b}$  quark pairs are predominantly produced in either forward or backward direction with respect to the beam direction and with only a small opening angle between them. The detector is therefore constructed as a spectrometer optimised for  $b$ -physics and is only instrumented in a small fraction of the full solid angle.

This chapter gives an overview of the detector, its subsystems, and the upgrade during the Long Shutdown 2, with a focus on the tracking system.

#### 3.1 The LHCb detector

The LHCb detector is a single-arm forward spectrometer that covers an angle of 300 mrad (250 mrad) in the horizontal bending (non-bending) plane of the magnet [18]. Figure 3.1 shows the detector and its subsystems in its original form, which operated from 2010 until the end of 2018 and recorded an amount of data corresponding to an integrated luminosity<sup>1</sup> of more than  $9 \text{ fb}^{-1}$  [19].

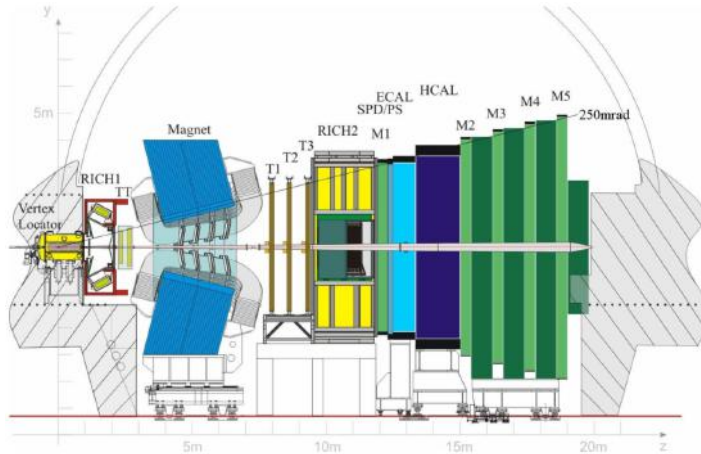


Figure 3.1: Schematic side view of the LHCb detector and its subsystems in its original form. LHCb uses a right-handed coordinate system with the beam pipe in  $z$ -direction and the vertical in  $y$ . Image from Ref. [18].

<sup>1</sup>The integrated luminosity  $\mathcal{L}_{int} = \int_0^T \mathcal{L}(t) dt$  is directly related to number of events of interest  $N = \mathcal{L}_{int} \cdot \sigma_p$ . With  $\sigma_p$  the production cross-section for the process of interest.

The different subdetectors of LHCb serve two main purposes: the tracking of particle trajectories and subsequent reconstruction of their momentum, and identification of the particle type. Together they provide the necessary information to reconstruct the underlying physics processes.

### 3.1.1 Tracking

The tracking system of LHCb, illustrated in Fig. 3.2, consists of the Vertex Locator (VELO) and four planar tracking stations: the Tracker Turicensis (TT) upstream of the magnet and the three T-stations downstream [18]. The magnet is a normal conducting dipole magnet with a bending power of 4 Tm in the  $xz$ -plane [18].

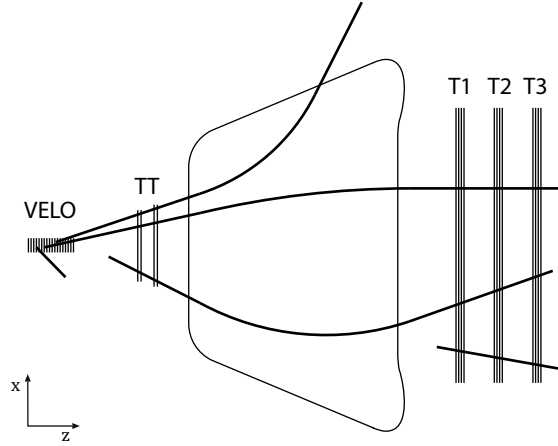


Figure 3.2: The LHCb tracking system. Image adapted from Ref. [20].

The momentum of a charged particle is reconstructed by measuring the deflection of its trajectory in a magnetic field. A particle with charge  $q$  and velocity  $\vec{v}$  travelling through a magnetic field  $\vec{B}$  will experience the Lorentz force

$$\vec{F} = \gamma m \dot{\vec{v}} = q (\vec{v} \times \vec{B}). \quad (3.1)$$

Assuming a homogenous magnetic field with only one component, the particle is forced on a helical orbit whose projection onto the bending plane of the magnet is a circle with radius  $R$

$$\frac{mv_T^2}{R} = qv_TB \Rightarrow R = \frac{p_T}{qB} \quad (3.2)$$

where  $v_T$  and  $p_T$  are the velocity and momentum components transverse to the magnetic field. The situation is illustrated in Fig. 3.3, where the right handed coordinate system of LHCb is adopted. By exploiting simple geometrical relations the measurement of  $p_T$  is translated into the measurement of the deflection angle  $\theta$

between the trajectory before and after the magnet. Assuming that the length  $L$  of the magnetic field is much smaller than the bending radius ( $L \ll R$ ) the transverse momentum is given by

$$p_T = \frac{qLB}{\theta}. \quad (3.3)$$

In order to measure  $\theta$ , at least two points before and after the magnet need to be measured.

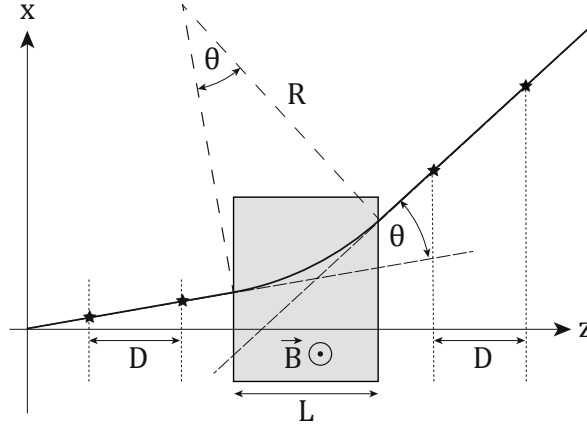


Figure 3.3: Particle trajectories are measured before and after the magnetic field. The deflection angle between the two straight lines allows to determine a particle's momentum. Image adapted from Ref. [21].

The resolution  $\sigma_x$  with which  $N$  points before and after the magnet are measured directly contributes to the momentum resolution

$$\left( \frac{\sigma_{p_T}}{p_T} \right)_{meas} \propto \frac{\sigma_x}{D} \sqrt{\frac{1}{N}} \quad (3.4)$$

where  $D$  is the distance between the pair of measured points along the  $z$ -axis. Since the particle is not travelling the distance  $L$  through vacuum but typically air, it is also affected by multiple Coulomb scattering. The contribution to the momentum resolution is proportional to the length  $L$  and the radiation length<sup>2</sup> of the material  $X_0$ .

$$\left( \frac{\sigma_{p_T}}{p_T} \right)_{ms} \propto \sqrt{L/X_0} \quad (3.5)$$

The overall momentum resolution is then given by the quadratic sum of both

<sup>2</sup>The radiation length characterises processes involving the Coulomb potential of atomic nuclei.

contributions. To optimise the momentum resolution the different dependences need to be considered.

$\propto \sigma_x$ : The detector resolution should be as small as possible until different effects, *e.g.* multiple scattering, dominate.

$\propto 1/\sqrt{N}$ : A large number of measurement points  $N$ , improves the resolution and helps with the pattern recognition in the track finding. In order to have a sufficiently large number of points given a certain number of detection layers, each layer is required to have a high hit efficiency.

$\propto 1/D$ : An increased distance, lever arm, between the points improves resolution.

These considerations, amongst other things, are reflected in the design of the different subdetectors that make up the LHCb tracking system. They result in an excellent momentum resolution, which for tracks traversing the full system is on the per mille level [10]. The detectors are presented in the following.

### **Vertex Locator**

The VELO is designed to track particle trajectories close to the interaction point and to reconstruct the displaced secondary vertices that are a distinct feature of  $b$ - and  $c$ -hadron decays [18]. The detector, as shown in Fig. 3.4, is composed of 42 submodules each containing a pair of radial ( $R$ ) and azimuthal ( $\phi$ ) 300  $\mu\text{m}$  thick silicon microstrip sensors placed at a distance of about 8 mm away from the beam axis. The strip pitch in the inner region is 40  $\mu\text{m}$  and radially increases to about 100  $\mu\text{m}$ . The whole detector is mounted inside a vacuum vessel that is separated from the LHC primary vacuum by a thin aluminium foil to minimise the material interactions of charged particles before they traverse the sensors. The silicon sensors are readout by a custom ASIC called Beetle [22].

The fine strip pitch, low material budget, large number of detector planes, and proximity to the interaction point result in a hit resolution of about 4  $\mu\text{m}$  and a hit efficiency of well above 99% [23]. This allows for reconstructing the primary and secondary vertices in the  $xy$ -plane with a resolution of about 13  $\mu\text{m}$  in  $x$  and 35  $\mu\text{m}$  in  $y$  [23].

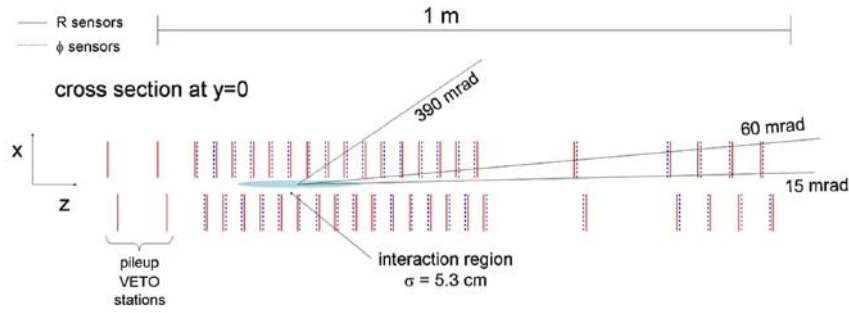


Figure 3.4: Cross section of the VELO in the  $xz$ -plane at  $y = 0$ . Image from Ref. [18].

### Tracker Turicensis

The TT, as shown in Fig. 3.5, is a 150 cm wide and 130 cm high planar silicon microstrip detector. It is composed of four detection layers ( $x, u, v, x$ ) where the  $u$  and  $v$  layers are tilted by  $-5^\circ$  and  $+5^\circ$ , respectively. The layers are further subdivided into halfmodules that contain seven silicon sensors with a strip pitch of  $183 \mu\text{m}$  and a stack of readout electronics at one end [18]. The four modules closest to the beam pipe are divided into three sectors (L, M, K), whereas the others are only divided into two sectors (L, M). Within the sectors L and M the strips of the sensors are bonded together, in sector K, where the occupancy is highest, a single sensor is used. Each of the sectors is read out by three Beetle chips. The resolution is around  $50 \mu\text{m}$  and the hit efficiency about 99.7% [10].

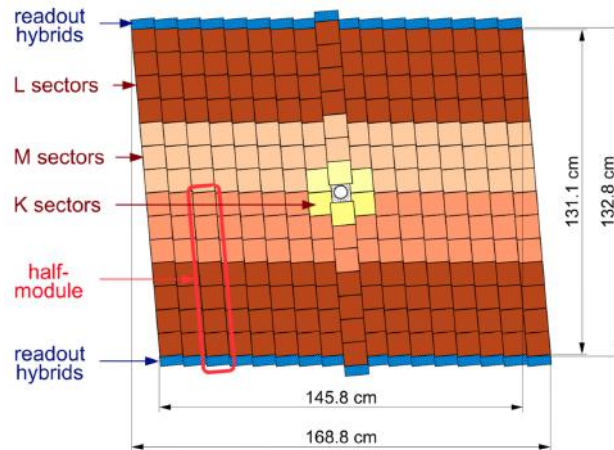


Figure 3.5: Layout of the third TT layer. The different readout sectors (L, M, K) are shown in different shades. Image from Ref. [18].

## T-stations

The three T-stations downstream of the magnet are composed of four detection layers using a  $x$ - $u$ - $v$ - $x$  geometry where the  $u$  and  $v$  layers are tilted by  $\pm 5^\circ$ . Figure 3.6 shows the layout of the three stations. The high occupancy region around the beam pipe is covered by the 120 cm wide and 40 cm high cross shaped Inner Tracker (IT). It uses silicon microstrip sensors with a strip pitch of  $198 \mu\text{m}$  readout by the Beetle chip and allows for reconstructing the hit position with a resolution of about  $50 \mu\text{m}$  and a hit efficiency of around 99.9% [10].

The outer region is covered by the Outer Tracker (OT), a drift-time detector which utilises 4.9 mm diameter straw-tubes filled with a mixture of Argon and  $\text{CO}_2$ . The hit positions are reconstructed based on the drift time of the ionisation charges left by the interaction of a passing particle with the gas. The OT reaches a resolution of  $170 \mu\text{m}$  and an efficiency of  $\geq 99.5\%$  [24, 25].

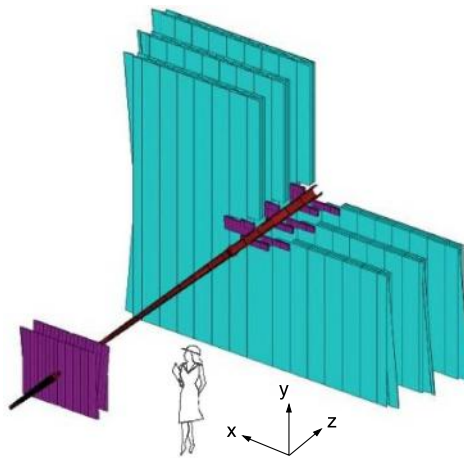


Figure 3.6: Schematic view of the LHCb tracking system without the VELO. The two silicon tracking detectors, TT and IT, are shown in purple. The straw-tube modules of the OT are shown in turquoise. Image from Ref. [18].

### 3.1.2 Particle identification

Particle identification in LHCb is provided by four subsystems: the two ring-imaging Cherenkov (RICH) detectors, the calorimeter system, and the muon stations. Each of the detectors exploit different phenomena which allow for distinguishing between specific types of particles.

#### Ring-imaging Cherenkov detectors

The role of the two ring-imaging Cherenkov detectors, RICH1 and RICH2, is the identification of charged hadrons, mainly pions, kaons, and protons. The discrimination between pions and kaons is particularly crucial since they are present in many decays of

$B$  and  $D$  mesons. The RICH detectors use the phenomenon of Cherenkov radiation to determine the particle type. A charged particle passing through a medium with a velocity larger than the speed of light in the medium emits Cherenkov radiation under a characteristic angle

$$\cos(\theta_C) = \frac{c}{nv} \quad (3.6)$$

where  $n$  is the refractive index of the medium. By measuring the angle and combining it with the momentum measurement the particle's mass can be inferred, as shown in Fig. 3.7. The two RICH detectors of LHCb are designed to cover the full momentum range. The detector before the magnet, RICH1, covers the low momenta from about 1 to 60 GeV/ $c$  using a  $C_4F_{10}$  radiator, while the detector behind the magnet, RICH2, covers the high momentum range from 15 GeV/ $c$  to above 100 GeV/ $c$  using a  $CF_4$  [18].

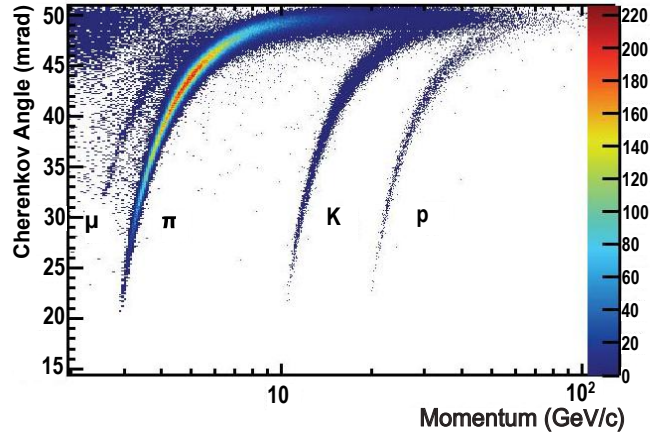


Figure 3.7: Cherenkov angle versus momentum for  $C_4F_{10}$  in RICH1. The different particle species follow distinct bands of constant mass. Image from Ref. [10].

### Calorimeter system

The calorimeter system is located downstream of RICH2 and provides the identification of electrons, photons, and hadrons, as well as a measurement of their energy and location [18]. High energetic particles interacting with dense matter produce cascades of lower energy particles that subsequently undergo further interactions until all energy is absorbed in the material. These cascades are known as particle showers and are categorised in either electromagnetic or hadronic showers, depending on whether the particle primarily interacts via the electromagnetic or strong interaction. The particle identification in the calorimeter system exploits the fact that the characteristic length on which the two types of showers evolve is vastly different. Electromagnetic showers are characterised by the radiation length  $X_0$  and hadronic

showers by the nuclear interaction length  $\lambda$ , with  $X_0 \ll \lambda$ .

The Electromagnetic Calorimeter (ECAL) together with the Scintillator Pad Detector (SPD) and Pre Shower (PS) in front of it, allows for distinguishing between neutral hadrons, electrons and photons. Charged particles passing through the SPD lead to the emission of fluorescent light in the scintillators [26], whereas neutral particles like photons or neutral pions pass it undetected. The PS contains a 15 mm thick lead absorber which causes mainly electrons and photons to shower. It provides an additional longitudinal segmentation to the calorimeters and allows for better separation of electrons and charged hadrons. The ECAL itself is composed of several alternating layers of lead and scintillator tiles with a total thickness of 42 cm, corresponding to  $25 X_0$ . [27]. The amount of light produced in the scintillator by the electrons in the electromagnetic shower is proportional to their energy. The last part of the calorimeter system is the Hadronic Calorimeter (HCAL), which uses a similar alternating structure of absorbers and scintillators as the ECAL. The HCAL, however, uses iron absorbers and has a total depth of about 1.3 m ( $5.6 \lambda$ ) [27].

### **Muon stations**

The identification of muons is fundamental to the physics goals of LHCb since they are present in the final states of many  $B$  and  $D$  decays. The muon system (M1–M5) is designed to provide a fast trigger on muons and subsequent identification. The first of the five muon stations is located upstream of the SPD and is used to improve the  $p_T$  measurement in the trigger [18]. The stations M2–M5 are located downstream of the calorimeters and are interleaved with 80 cm thick iron absorbers. The absorbers correspond to a total depth of approximately  $20 \lambda$  and reduce the hadronic background. Only high energetic muons with a momentum above 6 GeV/ $c$  are able to transverse all stations.

The muon stations use gas detectors, either multiwire proportional chambers (MWPCs [28]) or gas electron multipliers (GEMs [29]), that allow for reconstructing the position of a particle by tracking the ionisation it left behind.

## **3.2 The LHCb detector upgrade**

The LHCb detector will undergo a major upgrade during the LHC’s Long Shutdown 2 from 2019 to 2020 that will allow the experiment to exploit the full flavour-physics potential of the LHC [30]. To achieve this the upgraded detector will operate at an instantaneous luminosity of  $\mathcal{L} \approx 2 \times 10^{33} \text{ cm}^{-2} \text{ s}^{-1}$ , five times the previous value, and use a flexible online event selection. The LHC will also operate at its design value of  $\sqrt{s} = 14 \text{ TeV}$  centre-of-mass energy, which increases the production cross-sections of heavy quark flavours [12]. The current hardware trigger system, whose rate is currently limited to 1.1 MHz by the readout electronics of several subdetectors, will be replaced by a new software trigger that operates at 40 MHz and allows for feeding complete events every bunch crossing into the LHCb data acquisition farm [12].

This will improve the selection efficiency for a broad range of channels and the physics reach of the experiment. The upgrade is planned to operate for a period of ten years during which it will collect  $50 \text{ fb}^{-1}$  [30].

Removing the hardware trigger and operating the detector at 40 MHz requires the replacement of most frontend electronics and the data acquisition system. The increase in luminosity would result in a higher occupancy in the original detectors which, especially for the tracking detectors, leads to a degradation of the performance. The effect can be mitigated by increasing the granularity. A higher luminosity, also results in a higher radiation dose, which requires further changes to the active detector components as well as the frontend electronics.

## Tracking

The current VELO will be replaced by a pixel detector with electronics capable of a 40 MHz readout of the full system. The sensors are  $200 \mu\text{m}$  thick and feature pixels with a size of  $55 \times 55 \mu\text{m}^2$  [31]. The pixel technology is chosen due to its higher granularity and relative ease of pattern recognition [30]. The overall tracking performance is improved by moving the sensitive area even closer to the interaction region and reducing the material budget.

The tracking system upstream of the magnet will be replaced by the Upstream Tracker (UT). It uses the same geometry of four planes as the TT, but with larger coverage and thinner silicon microstrip sensors ( $250 \mu\text{m}$ ) [12]. Two types of sensors are used in the UT: the outer region is equipped with sensors that feature a strip pitch of  $190 \mu\text{m}$ , whereas in the innermost region of the detector sensors with a strip pitch of  $95 \mu\text{m}$  are used to cope with the occupancy.

The T-stations downstream of the magnet consisting of the IT and OT will be replaced by the Scintillating Fibre Tracker (SciFi Tracker). The detector uses 2.5 m long  $250 \mu\text{m}$  diameter scintillating fibres readout by silicon photomultipliers (SiPMs) outside of the acceptance. The SciFi Tracker is the focus of this thesis and described in more detail in Chap. 4.

## Particle identification

The overall structure of the RICH1 and RICH2 detectors will remain largely unchanged. However, the readout ASIC is directly bonded to the photodetectors and the whole assembly needs to be replaced to operate the detector at 40 MHz [32].

The calorimeter and muon systems do not require major hardware changes but several subcomponents, the SPD, PS, and the first muon station M1 will be removed. They played an import role in the hardware trigger and are no longer required in the upgrade [32].



## 4 The LHCb SciFi Tracker

In the upgrade the three T-stations downstream of the magnet will be replaced by a new detector based on scintillating fibres, the Scintillating Fibre Tracker (SciFi Tracker). This chapter describes the requirements, layout and various subcomponents of the LHCb SciFi Tracker.

### 4.1 Requirements

The T-stations downstream of the magnet are designed to provide standalone track reconstruction of charged particles, which, when combined with the information of the upstream tracking systems, allows for a precise measurement of the momentum. However, the momentum resolution for low momentum tracks ( $p \leq 80 \text{ GeV}/c$ ) is limited by multiple scattering, and by the detector resolution for higher momentum tracks [12]. The detector is therefore required to have a low material budget in the acceptance and high resolution in the bending plane of the magnet. The track reconstruction further requires a high hit efficiency in the detection layers. Finally, the upgraded detector has to be readout at 40 MHz and operate during the full lifetime of the upgrade. The main requirements of the upgrade of the T-stations are summarised as follows:

- The hit detection efficiency should be as large as possible ( $\approx 99\%$ ), while the fake hit rate should not exceed 10% of the signal rate at the same location [12].
- The single hit resolution must be  $< 100 \mu\text{m}$  in the bending plane of the magnet. A better resolution is not necessary as the extrapolation of tracks from the VELO is dominated by multiple scattering [12].
- The radiation length per layer must be  $X/X_0 \leq 1\%$  such that the effect of multiple scattering in the tracking layers is smaller than that of the material upstream of the magnet [12].
- The frontend electronics have to provide a triggerless readout of the full detector at 40 MHz and without any significant dead-time [12].
- The detector has to operate during the full lifetime of the upgrade and withstand an accumulated ionising radiation dose of up to 35 kGy near the beam pipe and a 1-MeV neutron-equivalent fluence of up to  $6 \times 10^{11} n_{\text{eq}}/\text{cm}^2$  at the position of the SiPMs [12].

## 4.2 Layout of the LHCb SciFi Tracker

The LHCb SciFi Tracker will occupy the same space as the OT and also follow the same layout of three stations composed of four layers in an  $x-u-v-x$  geometry where the two stereo layers ( $u, v$ ) are tilted by  $\pm 5^\circ$ . Each detection layer covers an area of approximately  $6 \times 5 \text{ m}^2$  and is made up of ten to twelve modules that each contain eight fibre mats. In total 128 modules will be used to construct the SciFi Tracker, covering an active area of more than  $320 \text{ m}^2$ . Figure 4.1 shows the layout of one SciFi Tracker station.

The fibre mats consist of six staggered layers of 2.5 m long,  $250 \mu\text{m}$  diameter scintillating fibres. The mats are readout by multichannel arrays of silicon photomultipliers (SiPMs) on one side, whereas a mirror is glued to the other side, facing the centre of the detector. All frontend electronics and services are located at the top and bottom of the detector outside of the acceptance.

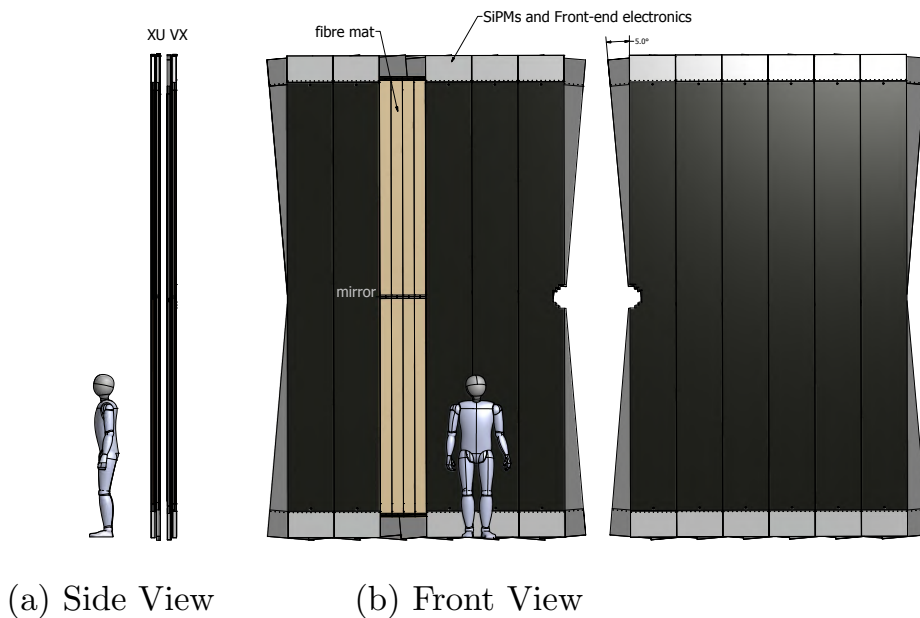


Figure 4.1: Layout of an LHCb SciFi Tracker station. Image from Ref. [33].

## 4.3 Working principle

The signal generation in the SciFi Tracker is illustrated in Fig. 4.2. When a charged particle crosses the scintillating fibres it deposits energy through ionisation which is subsequently transformed into light by the scintillation process [26]. A fraction of the light is trapped inside the fibres and transported via total internal reflection to the SiPMs where it is detected. The signal in each SiPM channel is proportional to

the number of detected photons. The particle position is calculated with a weighted mean of the channel signals.

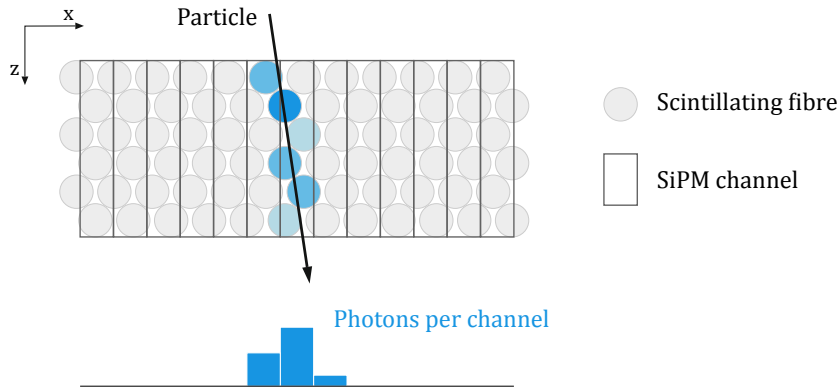


Figure 4.2: Illustration of the signal generation of a particle crossing a fibre mat. The coordinates corresponds to the right-handed coordinate system of LHCb.

## 4.4 Scintillating fibres

Scintillating fibres with a diameter of  $250\ \mu\text{m}$  of the type SCSF-78MJ from Kuraray<sup>1</sup> are used as the active component of the SciFi Tracker. They have been chosen due to their fast decay time of  $2.8\ \text{ns}$ , large attenuation length of  $> 3\ \text{m}$ , and high light yield [34, 35]. The fibres have a polystyrene core doped with a primary scintillator dye and a wavelength shifter and emit light in the range of  $400\ \text{to}\ 600\ \text{nm}$  [12].

When a charged particle traverses a fibre it deposits energy through ionisation which leads to the isotropic emission of scintillation light that is generated in a multistep process. First the ionisation energy deposited by the charged particle is absorbed by the polystyrene molecules and transferred to the primary dye through a non radiative dipole-dipole interaction called Förster transfer. The primary dye then subsequently releases the excitation energy through emission of photons (fluorescence) within a short time ( $\lesssim 1\ \text{ns}$ ) which is then reabsorbed by the secondary dye through either radiative or non-radiative processes [26]. The secondary dye acts as a wavelength shifter and emits photons at a longer wavelength such that re-absorption in the fibre is less likely to occur [12]. Photons emitted under the right angles are captured and guided through the fibre via total internal reflection. According to Snell's law the critical angle for total internal reflection at

<sup>1</sup>Kuraray Co. Ltd., Tokyo, Japan

the boundary of the materials with refractive indices  $n_1$  and  $n_2$  is given by

$$\theta_{crit} = \arcsin\left(\frac{n_2}{n_1}\right). \quad (4.1)$$

By using two claddings around the core of the fibre ( $n_{core} = 1.59$ ) with decreasing refractive indices of  $n_1 = 1.49$  and  $n_2 = 1.42$  about 5% of the light is captured [34]. The propagation time of the scintillation light is around 6 ns/m, due to the permittivity of the material and the fact that the photons undergo multiple reflections [12].

## 4.5 Fibre mats and modules

Each detection layer of the SciFi Tracker contains ten to twelve modules that each contain eight fibre mats, as well as all the necessary interfaces for the SiPMs and electronics.

### Fibre mats

The scintillating fibres described in the previous section are arranged into six staggered layers to form the fibre mats. The mats are produced with great precision and quality by winding them on a threaded winding wheel where the thread ensures an accurate positioning of the first fibre layer with a pitch of 275  $\mu\text{m}$ . All following layers then use the fibres below as positioning guide and are therefore shifted by half the pitch. During the winding process epoxy glue loaded with  $\text{TiO}_2$  is applied to hold the fibres together. The winding wheel in addition to the threads also features 2 mm deep grooves along its central line. The grooves are filled with epoxy before winding the first fibre layer and form alignment pins on the fibre mats after curing [36]. During assembly of the modules the pins ensure that the mats are straight and aligned with a precision of about 50  $\mu\text{m}$  in the  $x$ -direction [12].

After the winding process a series of steps are performed to finish the mats. First both sides are laminated with a black foil which increases their stability and also shields the fibres from light. Then polycarbonate pieces are glued to each end, and the mats are cut to obtain a high quality optical surface. Finally, a mirrored foil is glued to one end of the fibre mat.

### Fibre modules

A fibre module, as shown in Fig. 4.3, is the assembly of eight mats into a rigid object that can be mounted onto frames within LHCb and also provides interfaces for the SiPMs and frontend electronics [36]. The mats are sandwiched between a support structure of Nomex<sup>2</sup> honeycomb and carbon fibre reinforced polymer (CFRP). Two machined aluminium blocks (endplugs) are glued on either side that contain the

---

<sup>2</sup>Nomex is a registered trademark of E.I. du Pont de Nemours and Company (DuPont)

light injection system (see Sect. 4.8), and provide mounting points for the frontend electronics (Readout Box, ROB).

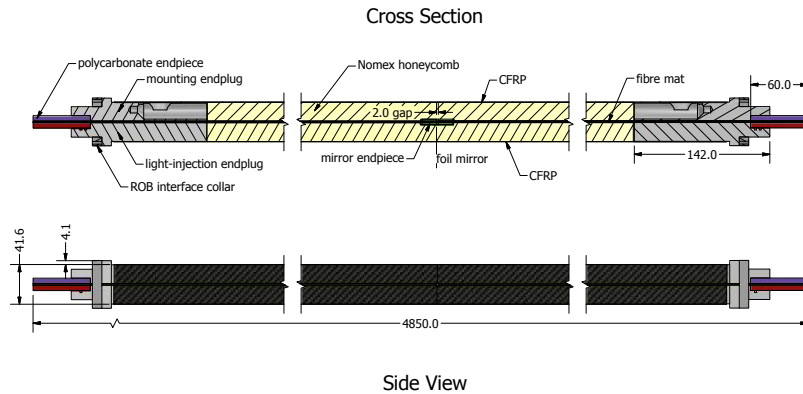


Figure 4.3: Schematic side view and cross section of a fibre module. Image from Ref. [36].

## 4.6 Silicon photomultipliers

Silicon photomultipliers are solid state photon detection devices that combine all the necessary features needed for the detection of photons in a high resolution scintillating fibre tracker [12]. They are composed of an array of geiger mode avalanche photodiode (G-APD) pixels connected in parallel.

The custom multichannel SiPM arrays for the LHCb SciFi Tracker, shown in Fig. 4.4, have been developed by Hamamatsu<sup>3</sup>. They feature 128 channels with a pitch of 250  $\mu\text{m}$  and height of 1.62 mm arranged on two silicon dies. Each channel consists of 104 rectangular pixels with a size of  $57.5 \times 62.5 \mu\text{m}^2$ . The SiPMs are sensitive to light with wavelengths from 300 to 700 nm [12], which matches the emission spectrum of the scintillating fibres (400–600 nm).

### 4.6.1 Working principle

All solid state photon detectors are based on a  $p$ - $n$  junction to which a reverse bias voltage is applied. At a  $p$ - $n$  junction an electric field and an area without free charge carriers, called the depletion zone, is formed. Photons incident on the depletion zone with an energy larger than the band gap of the semiconductor can create electron-hole pairs which are separated in the electric field and drift towards the anode and cathode. The thickness of the depletion zone can be increased by applying a voltage in the same direction as the electric field. In this case the junction is called reversed biased.

<sup>3</sup>Hamamatsu Photonics K.K.

A photodiode consisting out of a simple  $p-n$  junction however only produces a small signal due to the lack of amplification and is therefore not suited for low intensity applications. In an avalanche photodiode (APD) the problem is overcome by modifying the doping profile such that a high electric field is obtained. In the region of high electric field the primary photoelectrons are accelerated such that they have enough energy to create additional charge carriers, resulting in a multiplication of charges that produces a measurable signal.

When an APD is operated above its breakdown voltage, in so-called Geiger mode (G-APD), a photon creating an electron-hole pair in the depletion zone may trigger a self sustaining avalanche that leads to a permanent current at the diode. The avalanche needs to be terminated (quenched) which is typically done by a resistor in series (quench resistor) or an active quenching circuit.

The charge released in each avalanche is independent of the number of primary electron-hole pairs. The signal charge in a SiPM is therefore proportional to the number of pixels *i.e.* G-APDs where an avalanche occurred. As long as the number of photons incident on the SiPM is much smaller than the number of pixels, the probability of one pixel being hit by two photons is negligible, and hence the number of fired pixels is proportional to the number of detected photons. The amplitude of a SiPM signal is commonly given in units of photoelectrons (pe), where 1 pe corresponds to the signal of a single pixel.

## 4.6.2 SiPM characteristics

Silicon photomultipliers are characterised by a variety of different parameters with the most relevant described in the following.

### Breakdown voltage

The breakdown voltage ( $V_{BD}$ ) of a SiPM is defined as the bias voltage ( $V_{BIAS}$ ) where the electric field of the multiplication area becomes strong enough to trigger the creation of an avalanche. It is one of the most important parameters of a SiPM since many other parameters depend on the over voltage  $\Delta V = V_{BD} - V_{BIAS}$ . Due to production tolerances the breakdown voltage varies between different sensors of the same type which also affects the multi channel arrays of the LHCb SciFi Tracker. Each channel within one array has a different breakdown voltage, typically within  $\pm 300$  mV [37], which needs to be determined.

### Gain

The gain ( $G$ ), is the multiplication factor of the primary photoelectron in the avalanche. It is proportional to  $\Delta V$  and the capacitance of the pixel (junction capacitance,  $C_J$ ) [38]

$$G = \frac{Q_{Avalanche}}{e} = \frac{C_J \cdot \Delta V}{e}. \quad (4.2)$$

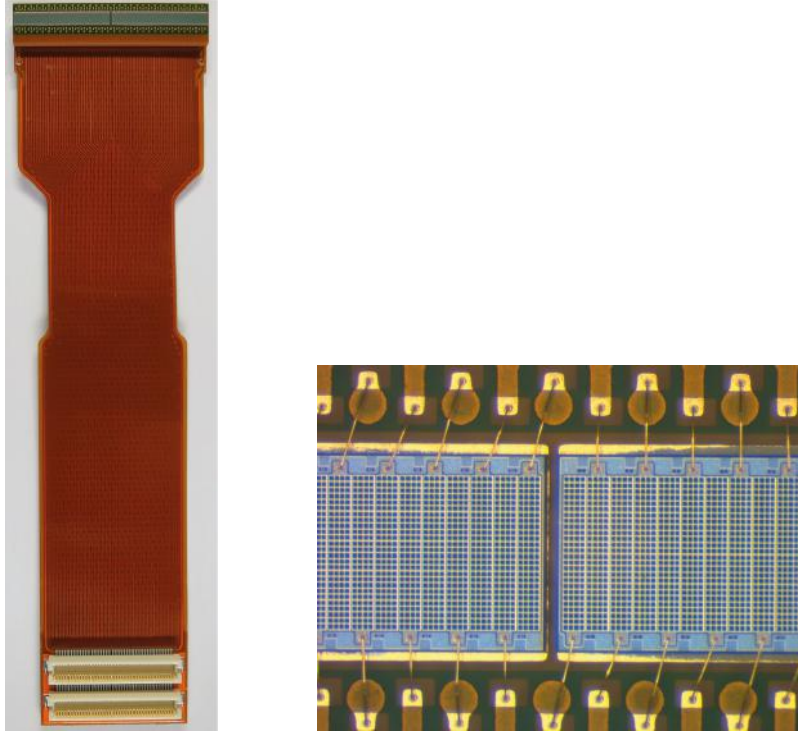


Figure 4.4: Hamamatsu 128 channel SiPM array mounted on a flexible carrier board and zoom on the active area showing the small gap between the two dies. Image from Ref. [37].

### Photon detection efficiency

The overall efficiency of a SiPM to detect a photon is called photon detection efficiency (PDE). It is the product of the silicon's quantum efficiency ( $QE$ ) times the ratio of sensitive to total area of the pixel (fill factor,  $f$ ), and the probability ( $P$ ) that an incoming photon triggers an avalanche [39]

$$PDE(\lambda, \Delta V) = f \cdot QE(\lambda) \cdot P(\lambda, \Delta V). \quad (4.3)$$

Both the quantum efficiency and the avalanche probability depend on the wavelength of the incident photon. The SiPM therefore needs to be optimised with respect to the emission spectrum of the scintillating fibres.

### Dark counts

Dark counts are random noise pulses due to thermally generated charge carriers in the depletion zone of the pixels. The rate of dark counts increases with temperature and also with the radiation dose due to bulk damage of the silicon which facilitates the thermal excitation of electrons and holes [39]. The SiPMs of the LHCb SciFi Tracker are expected to receive a dose of up to  $6 \times 10^{11} n_{\text{eq}}/\text{cm}^2$  after the life time of

the upgraded detector, which will significantly increase the dark count rate [12]. The rate however is approximately halved for every 10°C reduction in temperature [37]. By operating the SiPMs at -40°C the dark count rate is kept sufficiently low during the full time of operation.

In contrast to signals originating from the detection of a particle which produce signals in several neighbouring SiPM channels, dark counts are confined to single channels, which allows for an efficient suppression of the noise (see Sect. 4.9).

### Crosstalk

Crosstalk is noise correlated to the detection of a photon or dark count. Photons created during the avalanche process may reach neighbouring pixels and trigger another avalanche resulting in pulses produced simultaneously with the primary pulse [39]. For signals originating from the detection of a photon this is not a problem, however when coupled to dark counts, crosstalk creates fake signals with amplitudes larger than 1 pe.

### 4.6.3 Pulse shape

To illustrate the key characteristics of the SiPM pulse shape it is sufficient to look at the pulse of a single G-APD. Following Ref. [38], the pulse shape of a G-APD can be modelled with a simple equivalent electrical circuit shown in Fig. 4.5, where  $R_S$  is the resistance of the entire G-APD,  $R_Q$  the quenching resistor, and  $C_J$  the capacitance of the junction.

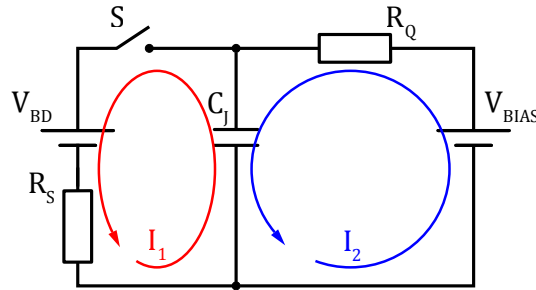


Figure 4.5: Basic equivalent circuit of a G-APD.

In the absence of light and ignoring dark counts the conceptual switch  $S$  is open, the voltage on the junction capacitor  $C_J$  is  $V_{BIAS}$ , and no current flows through the resistors.

As soon as a free charge carrier triggers an avalanche the switch is closed and the capacitor begins to discharge through  $R_S$ , which leads to a voltage drop at  $R_Q$  and a current ( $I_1$ ) through the terminals of the G-APD given by

$$I_1(t) \sim 1 - \exp[-t/(R_Q C_J)] = 1 - \exp(-t/\tau_S). \quad (4.4)$$

The current rapidly increases until  $t = t_{max} \approx 1$  ns where it reaches its maximum value of

$$I_{max} = (V_{BIAS} - V_{BD}) / (R_Q + R_S). \quad (4.5)$$

At  $t_{max}$  the voltage on the G-APD drops to approximately  $V_{BD}$ , the avalanche is quenched and the switch is open again. The junction capacitance begins to recharge across  $R_Q$  which leads to an exponentially decreasing current ( $I_2$ )

$$I_2(t) \sim -\exp(-t/\tau_Q). \quad (4.6)$$

The resulting pulse shape is sketched in Fig. 4.6. It is characterised by two time constants: a fast rise time

$$\tau_S = R_S \cdot C_J \approx 100 \text{ ps} \quad (4.7)$$

and a slow fall time

$$\tau_Q = R_Q \cdot C_J \approx 10 \text{ ns}. \quad (4.8)$$

For the latest version of SiPMs for the LHCb SciFi Tracker the time constants are  $\tau_S \leq 1$  ns and  $\tau_Q = 68$  ns [37].

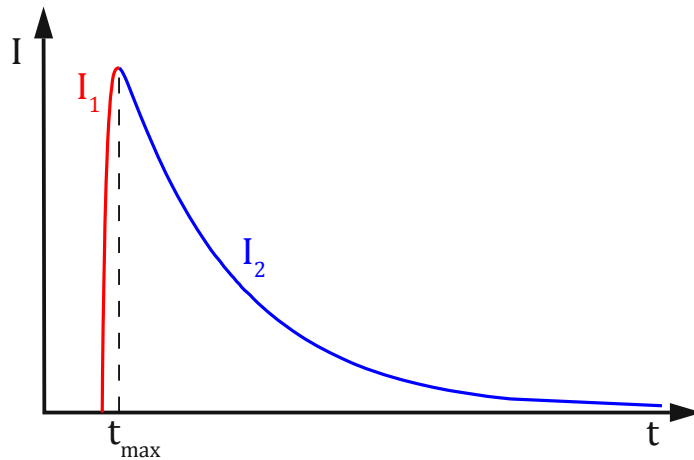


Figure 4.6: Illustration of the pulse shape of a G-APD with a fast component  $I_1$  and a slow component  $I_2$

## 4.6.4 SiPM pulse height spectrum

Pulse height ( $PH$ ) spectra recorded either in the dark or under pulsed illumination allow to determine the main performance parameters of SiPMs. In the context of the LHCb SciFi Tracker pulse height spectra recorded with the light from a pulsed laser are used to calibrate the frontend ASIC.

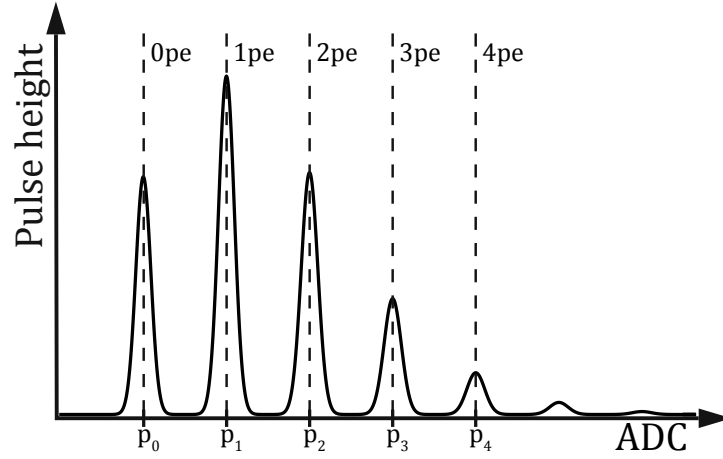


Figure 4.7: Illustration of the SiPM pulse height spectrum. The lines indicate the positions of the peaks  $p_k$ .

The pulse height spectrum of a SiPM, as shown in Fig. 4.7, is characterised by distinct peaks corresponding to 0, 1, 2 ...  $N$  geiger avalanches. It can be described by a sum of gaussian peaks with amplitude  $A_k$ , mean  $p_k$ , and width  $\sigma_k$ .

$$PH(x) = \sum_{k=0}^N A_k \cdot \frac{1}{\sqrt{2\pi\sigma_k^2}} \cdot \exp \left[ -\frac{(x - p_k)^2}{2\sigma_k^2} \right] \quad (4.9)$$

Assuming a linear behaviour of the digital to analog conversion (ADC), the position  $p_k$  of the peaks is determined by the pedestal position  $p_0$  and the gain per photoelectron  $G$  in units of ADC

$$p_k = p_0 + k \cdot G. \quad (4.10)$$

The width of the pedestal peak is given by the electronic noise of the system. In addition the width of the other peaks is widened due to differences in gain which are a result of slight variations in the capacitances of the pixels. The width of the  $k$ -th peak is then given by

$$\sigma_k^2 = \sigma_0^2 + k \cdot \sigma_1^2. \quad (4.11)$$

The number of incident photons approximately follows a Poisson distribution with mean  $\mu$  and determines the amplitude ( $A_k$ ) of the peaks. SiPMs however suffer

from crosstalk, which, following Ref. [40], can be modelled as a branching process where each primary avalanche produces a Poisson distributed number of avalanches in neighbouring pixels. This results in the so called Generalised Poisson (*GP*) distribution [41]

$$A_k = GP(k; \mu, \lambda) = \frac{\mu \cdot (\mu + k \cdot \lambda)^{k-1} \cdot \exp(-\mu - k \cdot \lambda)}{k!} \quad (4.12)$$

with the mean number of primary photoelectrons  $\mu$  and the number of crosstalk events  $\lambda$ .

## 4.7 Frontend electronics

The frontend electronics are directly connected to the fibre modules just outside of the detector acceptance. They are custom designed to process the SiPM signals with a readout frequency of 40 MHz and send the data to the data acquisition system. They are composed of three elements as illustrated in Fig. 4.8.

### PACIFIC

The PACIFIC is a custom 64-channel ASIC that shapes, integrates, and digitises the SiPM signals every 25 ns. The digitisation is based on three comparators which provide a 2-bit amplitude information of the integrated signals. A detailed description of the PACIFIC is given in Chap. 5.

### Cluster board

The digitised signals are sent to the cluster boards which feature two radiation tolerant Microsemi<sup>4</sup> IGLOO2 FPGAs (field programmable gate arrays) that each process the data of 128 PACIFIC channels [42]. The FPGAs run a fast clustering algorithm (see Sect. 4.9) to reconstruct the hit positions and to suppress noise.

### Master board

The clustered data is sent to the master board where it is encoded on dedicated GigaBit Transceiver (GBT [43]) ASICs and transmitted to the backend electronics via optical links. The master board also distributes the bias voltages to all circuits on the frontend boards and to the SiPMs, the timing commands needed to synchronise the electronics with the LHC collisions, and the control commands to configure the electronics. The low-voltage is supplied by Wiener<sup>5</sup> Maraton power supplies and converted to various voltages on the master board by radiation tolerant FEASTMP [44] DC/DC converters [42]. The high-voltage needed to bias the SiPMs is supplied

---

<sup>4</sup>Microsemi Corporation.

<sup>5</sup>W-IE-NE-R Power Electronics, GmbH.

by CAEN<sup>6</sup> modules and routed through the frontend electronics. Four SiPMs are supplied by one high-voltage channel.

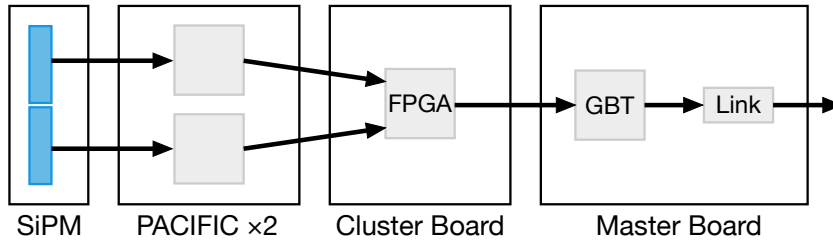


Figure 4.8: Schematic view of the frontend electronics. The data path is indicated by the arrows.

## 4.8 Light injection system

The light injection system (LIS) is used to calibrate the detector, in particular the thresholds of the PACIFIC, by injecting light pulses into the fibre mats. The system, as shown in Fig. 4.9, consists of a red vertical-cavity surface-emitting laser (VCSEL) driven by a GigaBit Laser Driver (GBLD [45]). The light is transmitted from the laser via a plastic optical fibre (POF). The last 13 cm, corresponding to the width of one fibre mat, has been scratched to allow the light to escape into a clear polycarbonate end-piece through which it then reaches the SiPMs. In order to have roughly the same light intensity in all fibre mats, each has its own VCSEL and light injection fibre.

The VCSEL was chosen over blue or UV-LEDs, because the latter require relatively high operational voltages that are not compatible with the GBLD [42]. The red light (670 nm) that is emitted by the VCSEL is detectable by the Hamamatsu SiPMs. The voltage pulse for the GBLD is generated on the master board and is synchronised to the PACIFIC sampling frequency with an adjustable phase of 0 to 25 ns. The light intensity can either be tuned by changing the modulation current of the GBLD, or by modifying the width of the pulse (see Sect. 6.5).

Most of the work carried out in the course of this thesis depended on the operation of this system and was either directly related to its performance or used it as a signal source.

## 4.9 Hit reconstruction

The increase in the dark count rate of the SiPMs due to irradiation will lead to an increasing number of fake hits in the detector that need to be avoided. In order

---

<sup>6</sup>CAEN S.p.A.

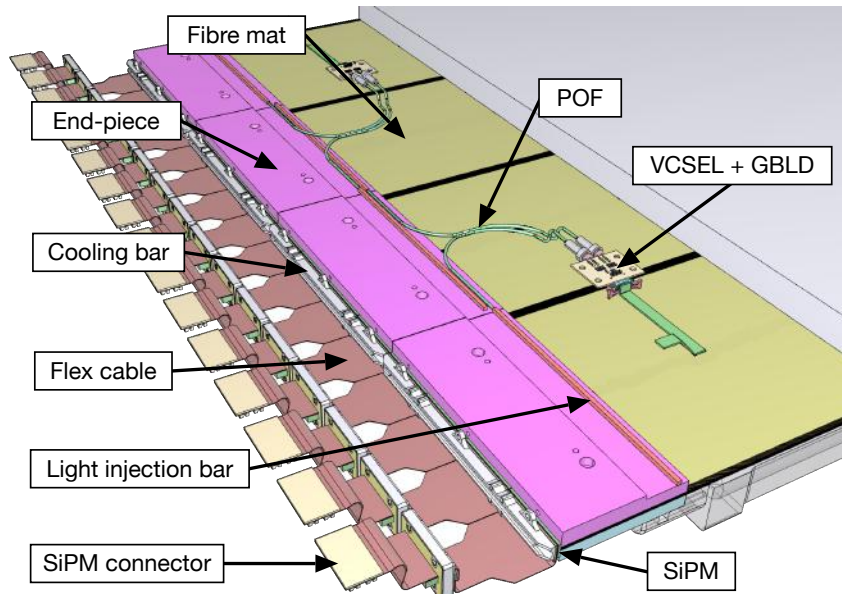


Figure 4.9: Schematic of the light injection system. Each fibre mat is equipped with its own light injection bar. Image adapted from Ref. [46].

to maintain the required tracking performance the fake hit rate should not exceed 2 MHz per SiPM array [12]. A clustering algorithm based on three thresholds is used to reduce the noise hits and to reconstruct the hit position.

### Clustering

A particle traversing the detector will typically leave a signal in several neighbouring SiPM channels. By combining the signals whose amplitude exceed certain comparator thresholds into clusters, the hit position can be reconstructed. The three thresholds, defined as *neighbour*, *seed*, and *high*, are set in ascending order with  $neighbour < seed < high$ , as illustrated in Fig. 4.10a. The amplitude in every channel can be represent by three bits according to which thresholds have been passed. However, due to the order of the thresholds only four combinations are valid (000, 001, 011, 111), which can be encoded in a 2-bit number (00, 01, 10, 11) to further reduce the amount of data.

The cluster finding algorithm starts by searching for cluster candidates where the channel passes the *seed* threshold. Signals from adjacent channels that pass the *neighbour* threshold are then included in the cluster. As illustrated in Fig. 4.10b, a valid cluster is finally accepted if one channel exceeds the *high* threshold or it contains at least on channel above the *seed* and one above the *neighbour* threshold.

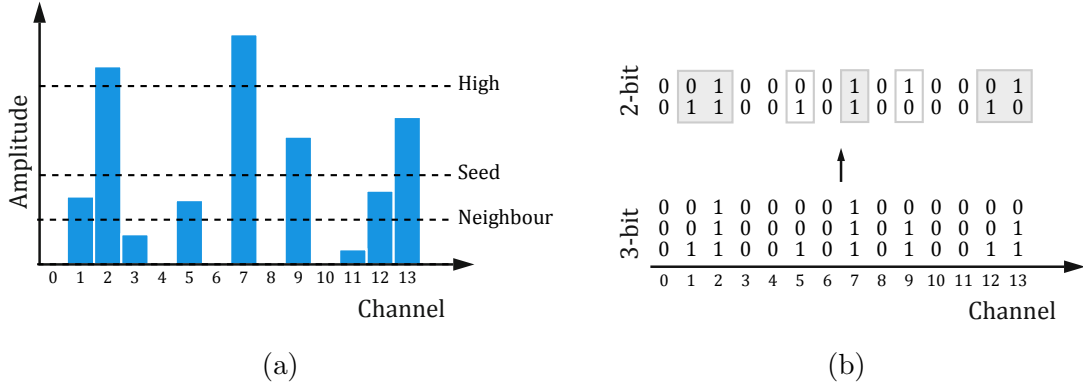


Figure 4.10: Illustration of the cluster finding algorithm based on the amplitude information given by three thresholds. Figure 4.10a shows the analogue SiPM signals and set thresholds, and Fig. 4.10b the corresponding digital output. The grey boxes illustrate found clusters and the open boxes rejected clusters. Image inspired from Ref. [35].

### Hit position

The hit position ( $\bar{x}$ ) is reconstructed by calculating the barycentre of the cluster using the weighted average

$$\bar{x} = \frac{\sum x_i \cdot w_i}{\sum w_i} \quad (4.13)$$

for channels  $i$  in the cluster with positions  $x_i$ , and weights  $w_i$  according to threshold passed. The weights do not necessarily correspond to the value of the threshold but can be adjusted to optimise the detector resolution.

## 5 The PACIFIC ASIC

The PACIFIC is the frontend ASIC of the LHCb SciFiTracker and includes all elements to amplify, shape, and digitise the SiPM signals. This chapter gives an overview of the main design and functional aspects of the chip and introduces the final version PACIFICr5q.

### 5.1 Design

The PACIFIC chip is a 64 channel ASIC designed for a 40 MHz triggerless readout of SiPMs. It has a low power consumption of less than 12 mW per channel and is developed using TSMC's<sup>1</sup> 130 nm process [47].

Each channel of the PACIFIC contains the analog processing chain shown in Fig. 5.1 consisting of four distinct functional blocks, which are described in the following.

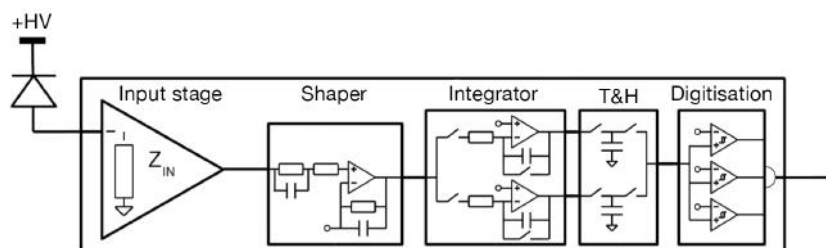


Figure 5.1: PACIFIC channel block diagram consisting of the input stage, a fast shaper, integrator and track-and-hold stage, and three comparators for digitisation. Image adapted from Ref. [47].

#### Input stage

The input stage is directly connected to the SiPM anode. It consists of a low impedance ( $\approx 50 \Omega$ ), high bandwidth ( $\approx 250$  MHz) current-mode amplifier with four selectable gains and a transimpedance amplifier which converts the current signal into a voltage. The input stage also allows for tuning the bias voltage of each SiPM channel within a range of 200–750 mV in steps of 50 mV to compensate for differences in the breakdown voltage. This ensures that every channel operates at the same over voltage and thus has the same gain and photon detection efficiency.

<sup>1</sup>Taiwan Semiconductor Manufacturing Company

## Fast shaper

The SiPM signals extend over several LHC bunch crossing periods mainly due to two effects: the light generation and propagation in the fibres, and the long tail of the SiPM pulses. The shaper suppresses the signal tail in order to minimise spillover into the next bunch crossing and to reduce the fluctuations of the integrated signal as a function of the signal arrival time [12]. By reducing the pulse duration to about 5 ns [48] (full width at half maximum, FWHM) the response of the integrator can be kept constant for a larger range of signal arrival times.

The implementation of the shaper contains a pole-zero cancellation for the slow time constant of the SiPM pulse that can be adjusted to account for different signal shapes. It is based on the simple circuit shown in Fig. 5.2.

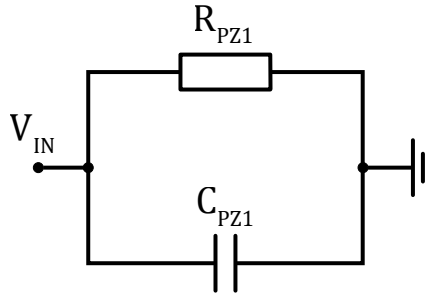


Figure 5.2: Basic circuit illustrating the pole-zero cancellation that determines the fall time of the shaped signal.

The impedance between the node  $V_{IN}$  and ground is

$$Z(\omega) = \frac{R_{PZ1}}{1 + i\omega R_{PZ1} C_{PZ1}} \quad (5.1)$$

with a pole at

$$\omega = \frac{i}{R_{PZ1} C_{PZ1}}. \quad (5.2)$$

The signal after the shaper then has a fall time given by

$$\tau = R_{PZ1} C_{PZ1}. \quad (5.3)$$

The fall time can be tuned from 0.3 to 18 ns by changing the values of the pole-zero resistor  $R_{PZ1}$  and capacitor  $C_{PZ1}$  [48].

## Integration

The shaped SiPM signals are integrated by two interleaved gated integrators switching at 40 MHz in order to avoid any dead time during acquisition [48]. The principle of

this arrangement is as follows: when the first integrator is working, the second one is disconnected from the input and being reset.

Due to tolerances in the manufacturing process, which introduce a mismatch between the transistors, the DC baseline of the two integrators of one channel can be different. Since the output of both integrators is digitised using the same three comparators a difference of the DC level at the output of each integrator could generate a wrong digital output. To compensate for this effect the DC baseline of each integrator can be tuned.

The integrator is followed by a track-and-hold stage which is switched together with the integrator and holds the accumulated signal charge prior to the digitisation.

## Digitisation

The integrated signal is digitised using three adjustable comparators which provide the necessary amplitude information for the clustering algorithm described in Sect. 4.9. The comparator thresholds are configurable for each channel individually, which is necessary due to large mismatches of the integrator DC baseline across different channels that can not be compensated. The threshold voltage of each comparator is controlled by an 8-bit DAC and needs to be calibrated to the corresponding SiPM channel. The calibration procedure is presented in Chap. 6.

## 5.2 PACIFICr5q, the production version ASIC

The PACIFIC chip has been in development since 2013 and went through several iterations. An 8-channel prototype was submitted in 2014 which included the full analog processing chain described in Sect. 5.1 and, after promising results, a 64 channel prototype was submitted in 2015 (PACIFICr3) [48]. The first two versions of the ASIC (PACIFICr1 and PACIFICr2) were developed in IBM<sup>2</sup> 130 nm technology but due to unclear long term availability, the design was migrated to TSMC 130 nm, starting with PACIFICr3 [48]. Two more versions of the ASIC (PACIFICr4 and PACIFICr5a) were issued in 2016 and 2017, respectively, which improved the uniformity, track-and-hold stage and the dynamic range of the comparators. Version 5a however needed some additional adjustments that were implemented in two versions, 5p and 5q. Version 5q in addition implements a redesigned track-and-hold stage (see Sect. 7.2.3) to reduce the spillover due to charge sharing in the ASIC.

PACIFICr5q marks the final version of the chip and became available in 2018. Its performance was first evaluated in the lab and later also in a test beam campaign, the results of which are discussed in Chap. 7.

---

<sup>2</sup>International Business Machines Corporation

## 5.2.1 Improvement in signal spillover

Spillover describes the process by which part of a signal associated to a real hit in one bunch crossing is measured in the next bunch crossing. If the spillover signals are large enough to form clusters they increase the rate of fake hits and severely affect the tracking performance.

Spillover in the PACIFIC is due to the generation and propagation time of the scintillation light in the fibres which introduces differences in the signal arrival time, and the pulse shape of the SiPM. The effects of both can be minimised by reducing the pulse shape. Additionally the design of the track-and-hold stage of the previous ASIC version (PACIFICr5a/5p), shown in Fig. 5.3, lead to a significant amount of charge sharing between consecutive bunch crossings.

The capacitors ( $C_1$ ,  $C_2$ ) are switched with a negated behaviour ( $clk$ ,  $\neg clk$ ) between the two integrator inputs and the single output. When integrator 1 is working its output  $V_1$  is connected to the capacitor  $C_1$  but disconnected from the output  $V_{out}$ , while the opposite is true for integrator 2. During the switching from integrator 1 to integrator 2 both capacitors are connected for a short amount of time which leads to about 25% of the charge from  $C_1$  spilling over to  $C_2$ . This large amount of charge sharing results in a probability of around 60% to detect a cluster in the bunch crossing after the signal at the same position [47].

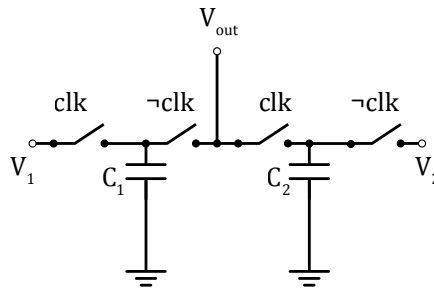


Figure 5.3: Schematic of the track-and-hold stage as implemented in PACIFICr5a and 5p. Image adapted from Ref. [48].

In order to address this problem PACIFICr5q employs a slightly different design which aims at reducing the analog charge sharing in the device. The new track-and-hold stage, shown in Fig. 5.4, relies on the generation of additional clock signals to operate the switches and introduces two additional switches that allow for disconnecting the capacitors. The capacitors are no longer switched together but slightly delayed with  $clk1 = clk2 + \Delta t$ . Additionally, the capacitor that is not in use is disconnected for a short amount of time ( $< 1$  ns) during the switching process. To eliminate the spillover completely the delay  $\Delta t$  and the time during which the capacitor is disconnected should be in the order of a few nanoseconds however this is not possible within the requirements of the PACIFIC to provide a 40 MHz readout with zero dead-time.

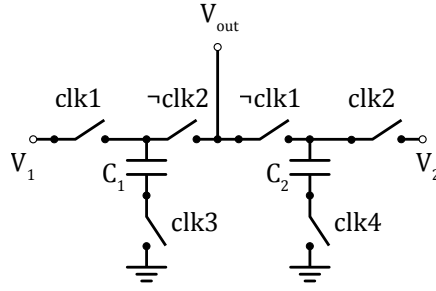


Figure 5.4: Schematic of the redesigned track-and-hold stage as implemented in PACIFICr5q. Image adapted from Ref. [47].

### 5.2.2 Shaper settings

The analogue processing chain, as described in Sect. 5.1, features a fast shaper with a tuneable pole-zero cancellation to remove the long tail of the SiPM signals. The parameters  $R_{PZ1}$  and  $C_{PZ1}$  that determine the fall time of the shaped SiPM signal are taken from a simulation of the ASIC which uses the measured pulse shape of the SiPM as input.

Two settings have been extracted from the simulation that aim to improve different performance aspects, the corresponding pulse shapes are shown in Fig. 5.5. Setting 1 ( $P_{PZ1} = 6$ ,  $C_{PZ1} = 11$ ) is optimised with regard to the detector efficiency. The shaped signal has a large amplitude and a very small amount of undershoot.

Setting 2 ( $P_{PZ1} = 5$ ,  $C_{PZ1} = 11$ ) on the other hand produces a shorter (faster) signal with a significant amount of undershoot which is subtracted from the signal during integration and should reduce the spillover in the next bunch crossing, it however also reduces the signal in the present bunch crossing.

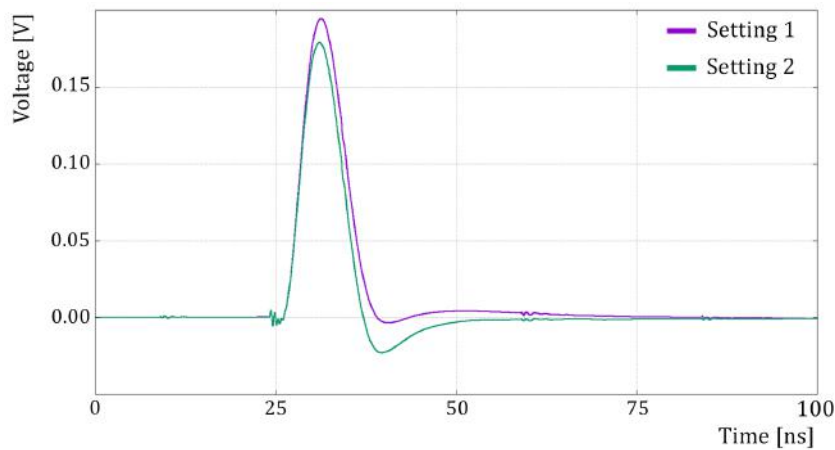


Figure 5.5: Simulation of the shaper output for two settings of the pole-zero parameters.



## 6 Calibration of the PACIFIC thresholds

The calibration of the PACIFIC comparators provides the conversion from a signal measured in units of DAC values to photoelectrons. The information is then used to set the comparator thresholds to the thresholds required by the clustering algorithm. This chapter describes the procedure to calibrate the comparator thresholds and presents a study of several factors that influence the calibration quality.

### 6.1 Threshold scan

To extract the calibration constants the complete SiPM spectrum under illumination, as shown in Fig. 6.1a, needs to be measured. This spectrum can only be directly measured by a full ADC which gives access to the complete amplitude information of each SiPM pulse. The PACIFIC on the other hand digitises the signals with three comparators, where the only information about the signal is, whether it is above or below a previously set threshold. The complete spectrum however can be measured by scanning through the threshold values and each time counting how many signals pass it. When the threshold is set below the pedestal peak all signals pass it and therefore the ratio is one. Each time a peak is being traversed fewer signals pass the threshold and the ratio continuously decreases until the threshold is in between two peaks giving rise to the characteristic stair case shape. The result of such a threshold scan is called *S-curve* and is illustrated in Fig. 6.1b.

The S-curve gives the probability that a signal  $X$  will exceed a certain threshold value  $x$ :  $P(X > x)$ , which corresponds to the complementary cumulative distribution function of the SiPM spectrum. Using Eq. 4.9 it is computed as

$$P(X > x) = 1 - \int PH(x) dx = 1 - \sum_{k=0}^N A_k(\mu, \lambda) \cdot \frac{1}{2} \left[ 1 + \operatorname{erf} \left( \frac{x - p_k}{\sigma_k \sqrt{2}} \right) \right]. \quad (6.1)$$

### 6.2 Threshold determination

The distinct peaks of the SiPM spectrum allow for excluding certain amplitudes by setting the threshold of the comparator in between two peaks, which in terms of the PACIFIC corresponds to the centre of a plateau. Calibrating the PACIFIC comparator thresholds requires finding these positions, which are denoted as  $p_{k.5}$  in the following.

A calibration tool has been developed in the course of this thesis, based on software

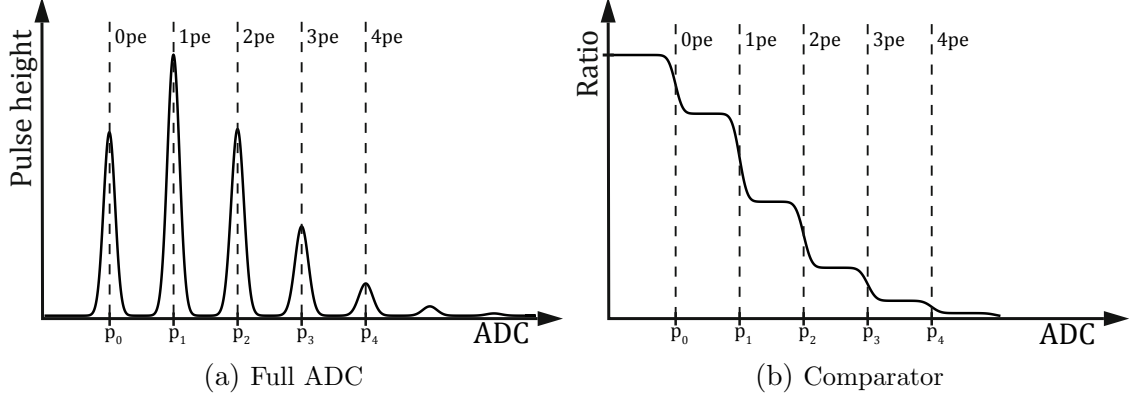


Figure 6.1: SiPM spectrum under pulsed illumination recorded with a full ADC and a single comparator. The dashed lines indicate the photoelectron peak (step) positions  $p_k$ .

originally written by Roman Greim for the calibration of a single PACIFIC. The implemented algorithms have been adapted and tuned for the latest PACIFIC and SiPMs versions and the software has been extended to be able to handle the calibration of 2048 channels corresponding to one side of a full SciFi Tracker module. The calibration procedure utilises the parametrisation of the threshold scan given by Eq. 6.1 and proceeds as follows.

In the first step the height of the 0.5 pe-plateau ( $P_{0.5}$ ) is determined, which allows to estimate the mean number of photons

$$\mu = -\ln(1 - P_{0.5}). \quad (6.2)$$

Given  $\mu$  and the average number of crosstalk events  $\lambda$ , the height  $P_{k.5}$  of the  $k$ -th plateau is calculate as

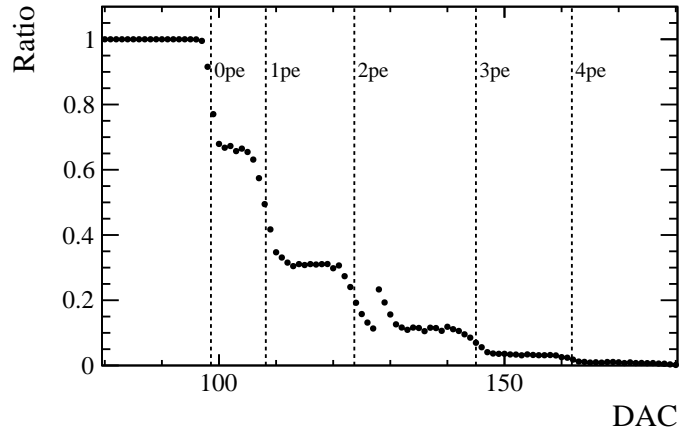
$$P_{k.5} = 1 - \sum_{i=0}^k A_i(\mu, \lambda). \quad (6.3)$$

The heights  $P_k$  of the transitions are then given by

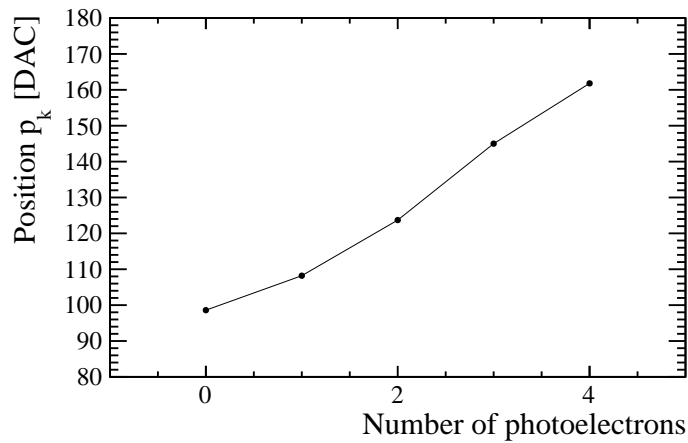
$$P_k = \frac{1}{2} (P_{(k-1).5} + P_{k.5}); \quad k > 0 \quad (6.4)$$

$$P_0 = \frac{1}{2} (1 + P_{0.5}). \quad (6.5)$$

Evaluating the S-curve at the heights  $P_k$  yields the step positions  $p_k$ , which in principle would allow for calculating the gain and therefore any  $p_k$  using Eq. 4.10. However, due to non-linear effects in the ASIC, shown in Fig. 6.2, this is not feasible. A parametrisation of these non-linearities proved to be not reliable enough and was therefore abandoned.



(a)



(b)

Figure 6.2: S-curve (6.2a) and corresponding step positions (6.2b) showing two non-linear effects: the 0.5 pe plateau is shorter, whereas the 2.5 pe plateau is widened due to a known discontinuity of the PACIFIC threshold DAC at a value of 127 [47].

In order to verify the determined positions  $p_k$ , a fit of the S-curve with Eq. 6.1 is performed. The parameters are either set to the values calculated above or to the initial values summarised in Table 6.1. Figure 6.3 shows an exemplary fit result. The

step positions are finally used to calculate the centre of the plateaus

$$p_{k.5} = \frac{1}{2} (p_k + p_{k+1}). \quad (6.6)$$

Table 6.1: S-curve fit parameters. Values marked with a minus sign are calculated from the threshold scan.

| Parameter  | Initial value | Fixed |
|------------|---------------|-------|
| $\mu$      | -             | No    |
| $\lambda$  | 0.03          | No    |
| $\sigma_0$ | 0.9           | No    |
| $\sigma_1$ | 0.5           | No    |
| $N$        | 6             | Yes   |
| $p_k$      | -             | No    |

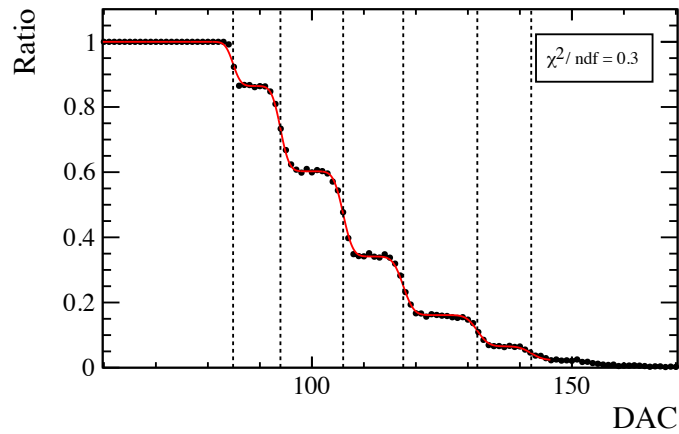


Figure 6.3: S-curve and fit result.

The calibration method has been tested on four datasets each containing the threshold scans for the three comparators of 2048 channels and only in about 1% of the cases fails to find the threshold positions. For the time being the channels where the calibration fails need to be calibrated manually. In the scope of the full SciFi Tracker 1% equates to more than 5000 incorrectly calibrated channels, which renders them either inefficient or inactive. Further studies to improve the reliability of the calibration algorithm are necessary.

## 6.3 Calibration quality

To ensure that the PACIFIC thresholds can be reliably calibrated using the method described in the previous section, the threshold scans have to be recorded under certain conditions. Three requirements have been identified during this thesis, which are described in the following.

### Integrator baseline trimming

As described in Sect. 5.1 the two integrators of each channel need to have the same DC baseline in order to yield the same comparator response. The process of aligning the baselines is called *trimming*. The trimming also has a profound effect on the quality of the recorded S-curves: if the baseline is not well trimmed the 0 pe plateau is often significantly shortened in one of the integrator's S-curves. A comparison of S-curves recorded with untrimmed and trimmed integrators is shown in Figure 6.4.

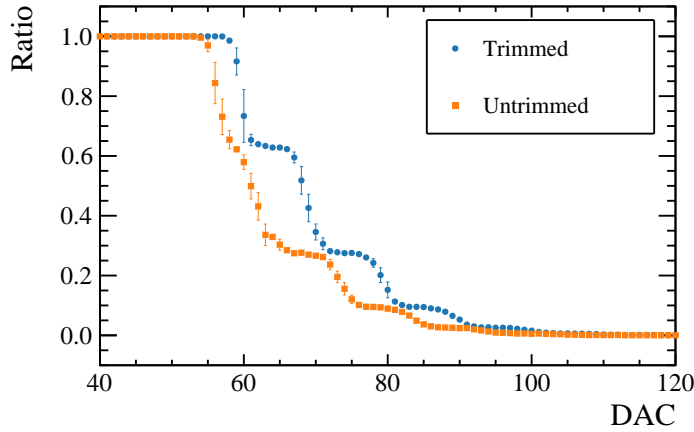


Figure 6.4: S-curves illustrating the effect of the integrator DC baseline trimming.

### Calibration light delay

The phase (delay) between the calibration light pulses, provided by the light injection system, and the PACIFIC readout clock has to be adjusted to ensure that the signals are maximally integrated. The optimal delay is determined by performing threshold scans at different delays and extracting the 1 pe signal amplitude in units of DAC, given by the difference between the positions of the first step and the pedestal. The amplitude as a function of the delay is shown in Fig. 6.5, where the maximum is found to be at a delay of 11 ns.

The S-curves for the optimal delay of 11 ns and a delay of 6 ns are shown in Fig. 6.6. At a delay of 11 ns the signal amplitude is largest and well separated from the noise, resulting in a S-curve with pronounced steps. At a delay of 6 ns the signal amplitude

is reduced, but since the noise is still the same, the separation between the signal and the noise is smaller. In the S-curve this leads to smeared out steps.

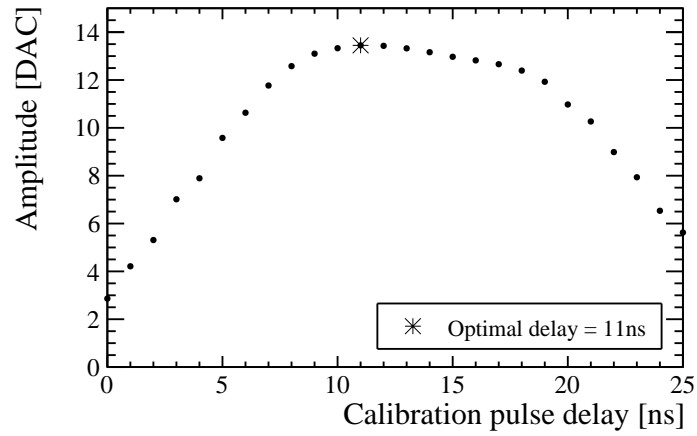


Figure 6.5: Single photon amplitude for different delays of the calibration light pulses.

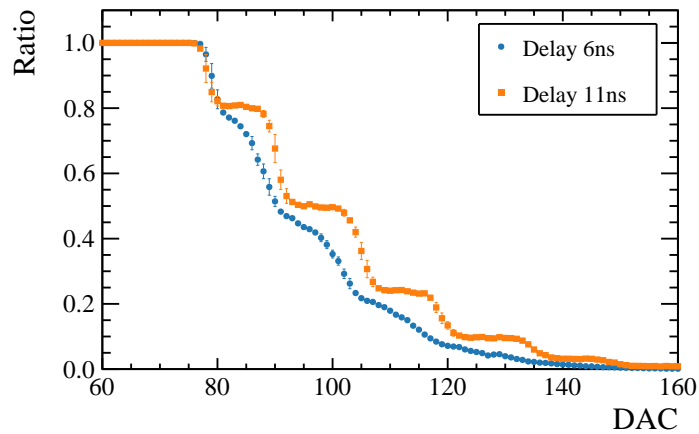


Figure 6.6: S-curves for two different delays of the calibration light pulses.

### Calibration light intensity

The intensity of the calibration pulses provided by the light injection system determines how many steps can be resolved in the S-curves. Figure 6.7 shows three S-curves recorded at different light intensities, corresponding to a mean number of photons ( $\mu$ ) of about 0.5, 1.5, and 4.5 pe, respectively. The intensity needs to be adjusted such that it is high enough to resolve the desired number of steps in the S-curve. For example, in order to resolve at least the 5 pe step, an intensity of about

1.5 pe is required. In addition, the intensity should also not exceed  $\sim 4$  pe, since this would introduce a shift of the PACIFIC integrator baseline.

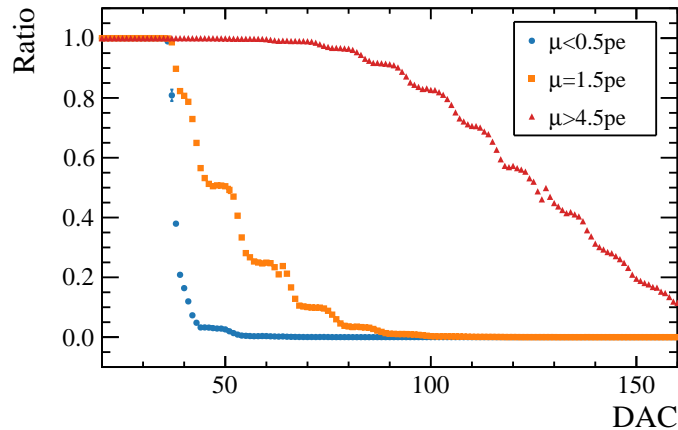


Figure 6.7: S-curves measured at different light intensities.

## 6.4 Low calibration light intensity

The intensity of the light pulses provided by the LIS is crucial for the calibration of the PACIFIC comparator thresholds. However, during quality assurance of the fibre modules it was discovered that a few of them showed a too low calibration light intensity even when the modulation current of the laser driver was set to the maximum.

As mentioned in Sect. 4.5 the fibre mats are cast in a black foil to increase their stability and to protect them from light. On one side the full length of the mat is covered by the foil, whereas it should stop at the polycarbonate pieces (endpieces) on the other side to expose the fibres to the light injection bar that sits right on top. The interface between the light injection bar and the fibre mat is illustrated in Fig. 6.8. Some fibre mats, however, have been produced with the black foil extending a couple millimetres under the endpiece as shown in Fig. 6.9. The foil could absorb some of the calibration light and reduce the intensity measured at the SiPMs. In order to verify this hypothesis, the calibration light intensity has been measured using four different mats with different lengths of black foil extending into the endpiece (0 mm, 5 mm, 8 mm, and 10 mm).

### Experimental setup

The measurement setup, shown in Fig. 6.10, consists of either one of the four aforementioned fibre mats, a light injection system, one SiPM, and a data acquisition system (DAQ) with a single PACIFIC. The light injection bar was mounted at the

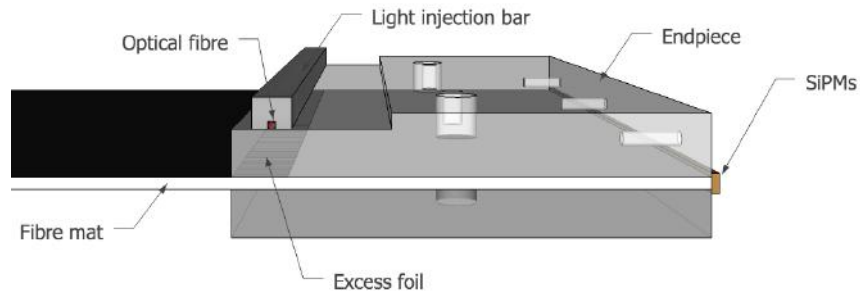


Figure 6.8: Illustration of the interface between the fibre mat and the light injection bar.

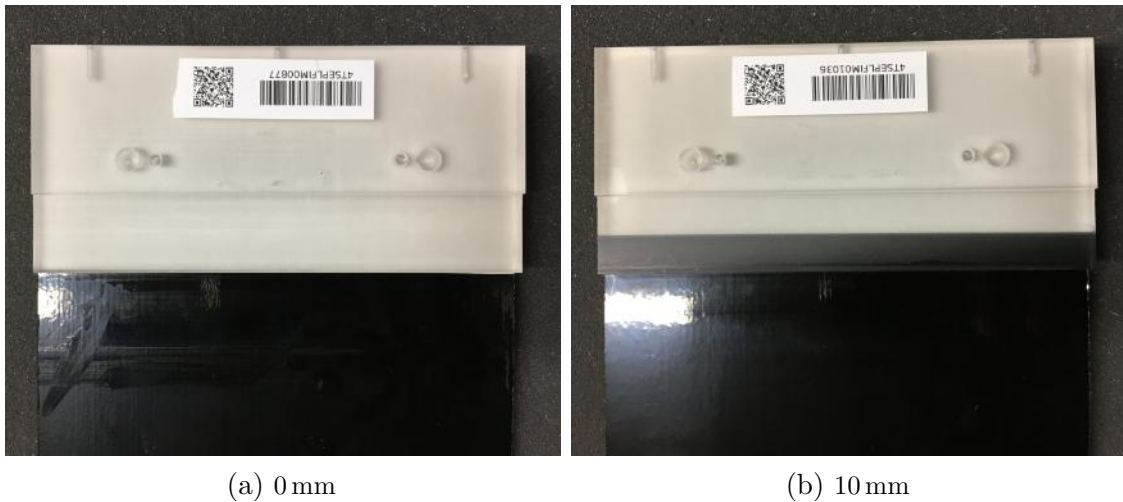


Figure 6.9: Fibre mats with 0 mm and 10 mm of excess black foil under the polycarbonate endpiece.

same position as it is in the fibre modules and the modulation current of the GBLD was kept constant throughout the measurements. The light injection system was triggered by the DAQ.

## Result

For each mat S-curves have been recorded from which the intensity, given by the mean number of photons ( $\mu$ ), is determined based on the calibration procedure discussed in Sect. 6.2. The measured light intensity as a function of the excess foil length is shown in Fig. 6.11, where a significant reduction of the intensity for an increasing length of foil is observed. The rate of the intensity reduction ( $\Delta\mu$ ) is computed by fitting a linear function to the data and is given by the slope of the function. A decrease of  $\Delta\mu = -0.07 \text{ pe/mm}$  is observed.

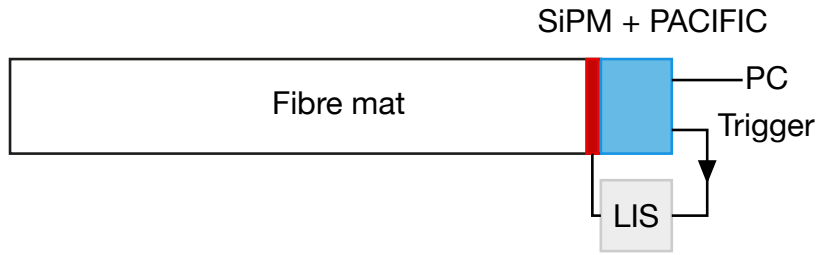


Figure 6.10: Schematic of the setup to measure the calibration light intensity for different fibre mats.

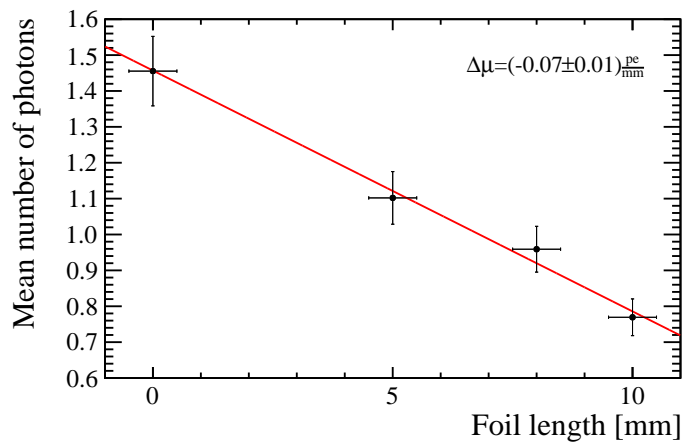


Figure 6.11: Calibration light intensity (mean number of photons) as a function of the excess black foil under the fibre mat polycarbonate piece. A linear fit was performed to determine the reduction rate  $\Delta\mu$ .

## 6.5 Increasing the light intensity

The generator of the voltage pulses in the LIS is originally specified to provide pulses with a fixed duration of 5 ns. It was, however, suggested that the light intensity can be increased by increasing the pulse width, which would allow to compensate the reduction of the intensity due to an excess of foil in the fibre mats.

### Experimental setup

In order to study the influence of the pulse width on the calibration light intensity, the build in pulse generator of the light injection system has been replaced by an external one, which allowed for adjusting the pulse width. The setup is illustrated in Fig. 6.12 and consisted of one fibre mat readout by one SiPM, a light injection system

with a single laser diode, the pulse generator, and the single-ASIC DAQ system.

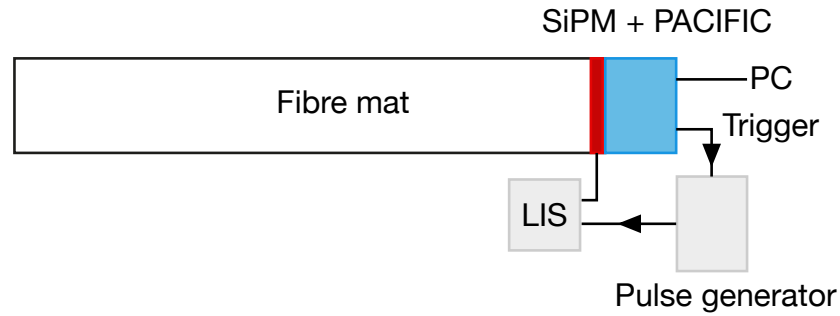


Figure 6.12: Schematic of the setup to measure the calibration light intensity as a function of the pulse width.

## Result

The measured intensity as a function of the pulse width is shown in Fig. 6.13. For widths up to 20 ns the intensity was found to increase linearly with a rate of  $\Delta\mu = 0.089 \text{ pe/ns}$  and beyond 20 ns with a rate of  $\Delta\mu = 0.144 \text{ pe/ns}$ . The values are however only valid for the used VCSEL and a dedicated study with a larger sample size is necessary to determine the values for  $\Delta\mu$ .

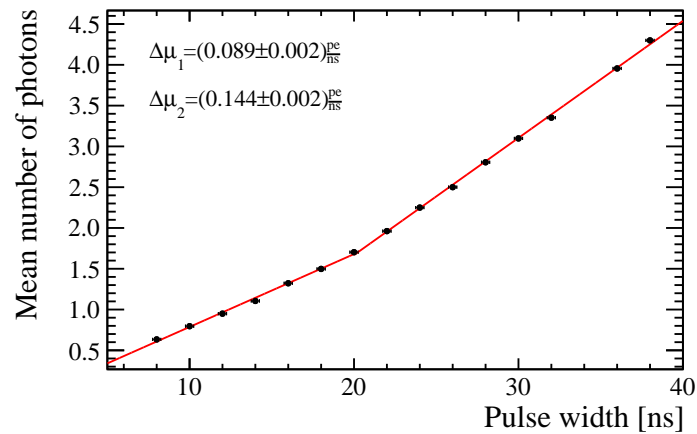


Figure 6.13: Calibration light intensity for different calibration pulse widths.

## 7 Performance of PACIFICr5q

This chapter presents studies of the performance of PACIFICr5q which aim to verify the new design of the track-and-hold stage as well as the influence of the two shaper settings. The integrator response was studied in the lab prior to a test beam campaign where the tracking performance of prototypes of the SciFi Tracker with PACIFICr5q has been investigated.

### 7.1 Integrator response

Due to the generation and propagation of the light in the fibres, the signals in the SciFi Tracker will arrive at different times at the SiPMs depending on where along the fibres they originate from. In order to keep a high efficiency over a large area of the detector, the integrator response has to be constant for a large range of signal arrival times.

#### Experimental setup

The integrator response was studied by performing threshold scans and calculating the single photoelectron amplitude in units of DAC for different delays of the calibration light pulse. The single photon amplitude is given by the difference between the positions of the first step and the pedestal. The setup is shown in Fig. 7.1 and consisted of a fibre mat equipped with four SiPMs, the light injection system, a programmable delay unit. Only one SiPM was connected to the PACIFIC DAQ system, which also provided the trigger signals to the light injection system.

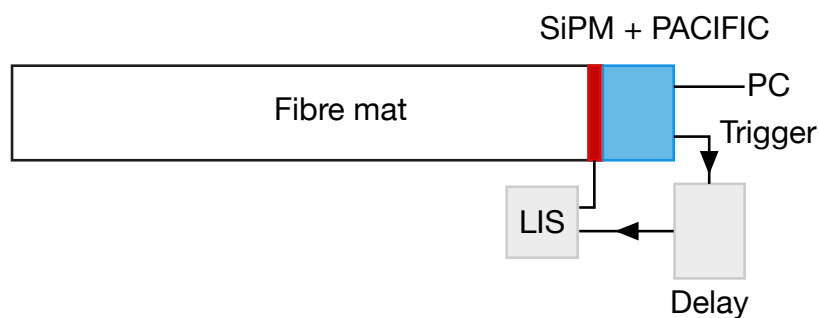


Figure 7.1: Schematic of the lab setup using the LIS as signal source.

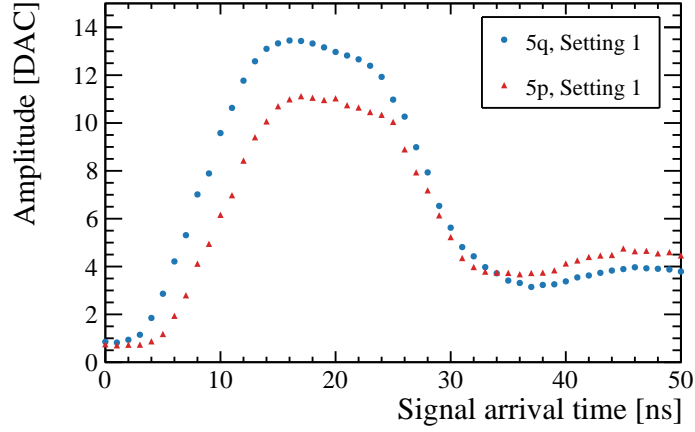


Figure 7.2: Response of the PACIFIC integrator in version 5q and 5p.

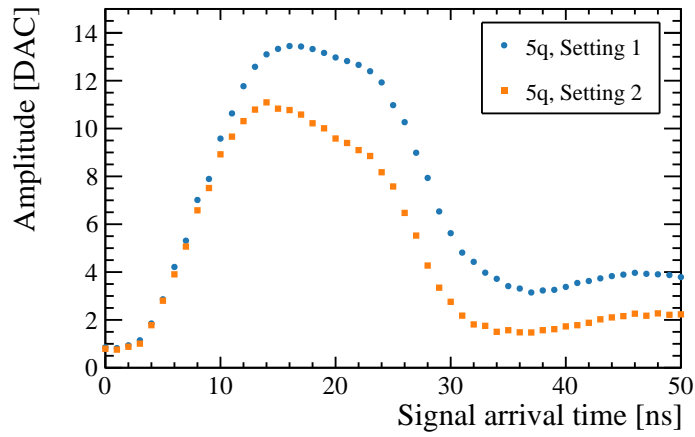


Figure 7.3: Response of the PACIFIC integrator for shaper settings 1 and 2.

## Result

The integrator response over two consecutive bunch crossings for PACIFIC versions 5p and 5q is shown in Fig. 7.2. The only difference between the two ASIC versions is the redesigned track-and-hold stage in 5q, where the reduction in charge sharing leads to a 30% increase of the amplitude. The width of the integration window is 11 ns for both versions.

The integrator response of PACIFICr5q for the two shaper settings is shown in Fig. 7.3. Setting 1 exhibits a maximum amplitude of around 13 DAC and a integration window (FWHM) of 11 ns. The faster shaping of Setting 2 leads to a reduction of 15% in the signal amplitude and a narrower integration window of 7 ns.

Table 7.1: Maximum amplitude and integration window size (FWHM) for PACIFIC versions 5p and 5q, and both shaper settings.

| Version | Setting | Amplitude [DAC] | Integration window [ns] |
|---------|---------|-----------------|-------------------------|
| 5p      | 1       | $11.1 \pm 0.4$  | $11 \pm 1$              |
| 5q      | 1       | $13.5 \pm 0.4$  | $11 \pm 1$              |
| 5q      | 2       | $11.1 \pm 0.4$  | $7 \pm 1$               |

## 7.2 Tracking performance

The individual components of the SciFi Tracker, *e.g.* prototype fibre modules, and previous SiPM and PACIFIC versions, have been intensively studied in previous years during several test beam campaigns which provided vital input during the development phase of the detector. Since the development of all subcomponents is effectively finished, the goal of the latest test beam campaign was to study the full system performance of prototypes of the SciFi Tracker. It was conducted at the CERN SPS<sup>1</sup> North Area in July 2018.

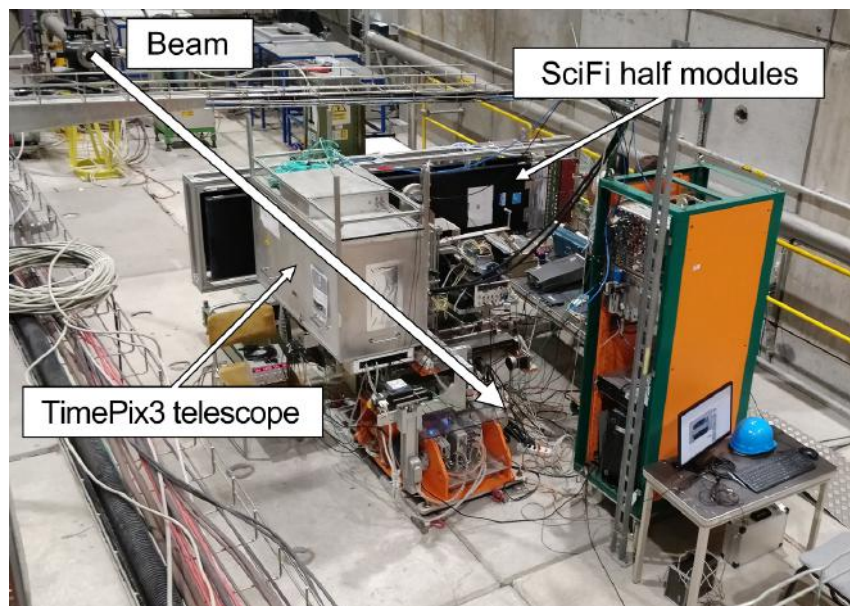


Figure 7.4: Picture of the test beam setup at the CERN North Area in July 2018. The beam first traverses the two SciFi half modules and then goes through the TimePix3 telescope.

<sup>1</sup>The Super Proton Synchrotron (SPS) is part of CERN's accelerator complex. It is used as the final injector for the LHC and provides the beam for several fixed target experiments and the test beam areas located in the CERN North Area.

## Experimental setup

The experimental setup, shown in Fig. 7.4, consisted of two production version full width but half length SciFi Tracker modules, each fully equipped with 16 SiPMs. The 4096 SiPM channels were read out by the complete chain of frontend electronics, as described in Sect. 4.7, and the data was recorded by a prototype version of the new DAQ system [49] developed for the LHCb experiment.

The TimePix3 [50] telescope was used to provide the reference tracks for the performance studies of the SciFi Tracker modules, as well as a fine timestamps which records the trigger time relative to the 40 MHz readout of the SciFi Tracker.

The beam was set to a width of about 1 cm and contained mainly pions and protons with a momentum of around 180 GeV.

## Event selection

The readout electronics of the SciFi Tracker are designed to operate in sync with the LHC bunch crossing frequency of 40 MHz, which precisely determines the arrival time of the particles. In contrast to the LHC, the SPS delivers five second long spills of particles to the test beam areas which arrive asynchronously with respect to the 40 MHz sampling frequency of the readout electronics. In order to study the performance of the SciFi Tracker modules the arrival time of the signal was recorded by the TimePix3 telescope. The delay between the trigger and the DAQ was adjusted such that most signals are recorded in one bunch crossing, as shown in Fig. 7.5. Within this bunch crossing the signals need to be selected based on their arrival time to ensure that they are properly integrated by the PACIFIC. Signals arriving either too late or too early do not fall into the efficient part of the integration window of the PACIFIC, are only partially integrated and therefore have a lower probability to pass a fixed threshold. Figure 7.6 shows the number of signals in all channels over the *high* threshold in the signal bunch crossing (corresponding to *BX2* of Fig. 7.5) for different signal arrival times.

At the maximum of the distribution, the signals are maximally integrated and have the highest probability to surpass a fixed threshold. Normalising to this maximum then allows for calculating the range of arrival times  $t$ , where the signals have a relative probability of  $P(t_0 < t < t_1) \geq X$  to pass the threshold.

## Clustering

The measurements presented in the following sections use data sets where no clustering was performed on the dedicated FPGAs but instead the full 2-bit amplitude information of each channel was recorded. To reconstruct the hit positions an offline clustering was performed using the algorithm explained in Sect. 4.9. The PACIFIC thresholds were set to *neighbour* = 1.5 pe, *seed* = 2.5 pe, and *high* = 4.5 pe with weights  $w_{neighbour} = 1$ ,  $w_{seed} = 2$ , and  $w_{high} = 6$ .

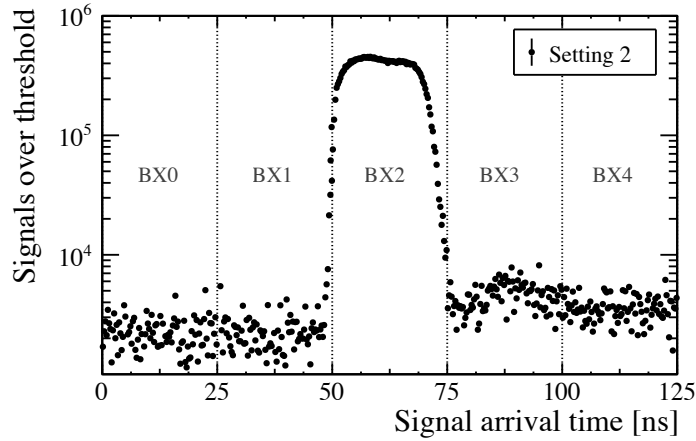


Figure 7.5: Distribution of signals over the *high* threshold for five consecutive bunch crossings.

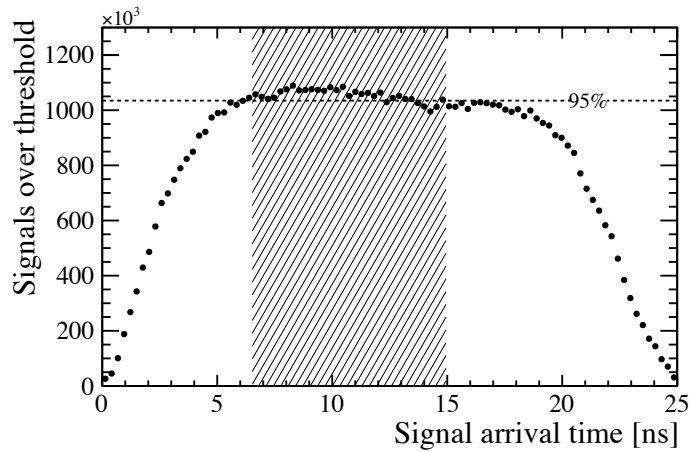


Figure 7.6: Distribution of the number of signals over the *high* threshold in the signal bunch crossing. The 95% level, relative to the maximum number of events, is shown as dotted line and the range of selected arrival times is indicated by the hatched box.

### 7.2.1 Hit efficiency

The efficiency to detect a charged particle traversing one detector layer is called hit efficiency. It is a crucial parameter since it directly affects the tracking efficiency and eventually the physics performance of the LHCb experiment.

The hit efficiency is calculated from the number of detected particles  $N_{SciFi}$ , *i.e.* reconstructed clusters, over the total number of particles  $N$  passing the detector at

a certain position  $x$ :

$$\varepsilon_{hit}(x) = \frac{N_{SciFi}(x)}{N(x)} \quad (7.1)$$

where the number of expected hits  $N(x)$  and the location  $x$  is given by extrapolating the telescope tracks to the position of the SciFi modules.

Figure 7.7 shows the measured hit efficiency as a function of the channel number for the width of one fibre mat. The beam was incident close to the mirror side of the mat and pointed at nine different positions along its width. However, since the beam was only about 1 cm wide there are channels where no data was recorded. Every 64 channels a drop in the efficiency, due to the gaps between the two dies of one SiPM and between different SiPMs, is observed. For the two channels around the small gap ( $220 \mu\text{m}$  [37]) in between the SiPM dies the efficiency drops to around 85% and for the larger gap ( $460 \mu\text{m}$  [12]) between two SiPMs it drops to 64%. The efficiency in the plateau region, *i.e.* all channels except the ones right next to the gaps, is found to be 99%. The averaged efficiencies are summarised in Table 7.2.

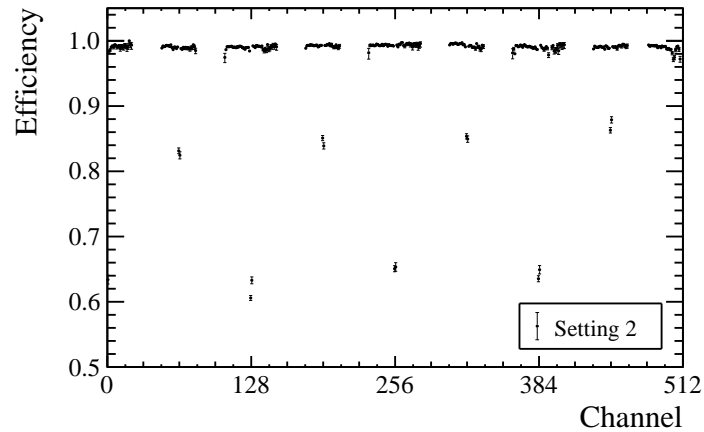


Figure 7.7: Hit efficiency at the mirror side of one fibre mat.

Table 7.2: Efficiency for channels in the plateau regions and at the two gaps.

|                | Plateau        | Die gap    | SiPM gap   |
|----------------|----------------|------------|------------|
| Efficiency [%] | $99.0 \pm 0.5$ | $85 \pm 2$ | $64 \pm 2$ |

## 7.2.2 Hit resolution

The predicted hit position ( $x$ ), given by the telescope tracks, is compared to the reconstructed hit position in the SciFi module ( $x_{SciFi}$ ) by calculating the residual

$$R = x - x_{SciFi}. \quad (7.2)$$

The resulting residual distribution is shown in Figure 7.8. The width  $\sigma_{residual}$  of the distribution is the quadratic sum of the track resolution  $\sigma_{track}$  and the single-hit resolution of the SciFi Tracker module  $\sigma_{SciFi}$

$$\sigma_{residual} = \sqrt{\sigma_{track}^2 + \sigma_{SciFi}^2} \approx \sigma_{SciFi}. \quad (7.3)$$

The resolution of the TimePix3 telescope is expected to be about  $10 \mu\text{m}$  [50] at the location of the SciFi Tracker modules, and is not assumed to significantly contribute to the measured residual width. The resolution of the SciFi Tracker is therefore approximately equal to the residual width.

The distribution is parametrised with a double Gaussian

$$F(R) \propto f \cdot \exp\left[-\frac{(R - \mu)^2}{2\sigma_{inner}^2}\right] + (1 - f) \cdot \exp\left[-\frac{(R - \mu)^2}{2\sigma_{outer}^2}\right] \quad (7.4)$$

where  $f$  is the fraction of entries in the inner gaussian and is typically around 98%. The broad outer distribution is likely due to scattering on the beam instrumentation in front of the setup. The two widths  $\sigma_{inner}$  and  $\sigma_{outer}$  can be combined to form an effective residual width where the two components are weighted by their relative contribution

$$\sigma_{eff} = \sqrt{f \cdot \sigma_{inner}^2 + (1 - f) \cdot \sigma_{outer}^2} \approx \sigma_{SciFi}. \quad (7.5)$$

The effective width gives a good estimate of the detector resolution and is measured to be  $65 \mu\text{m}$ , it however still includes the uncertainty from the track ( $\sigma_{track}$ ). To subtract this contribution a more detailed study of the telescope is necessary.

## 7.2.3 Spillover probability

The spillover probability is the probability to find a cluster at the same position in the bunch crossing following the signal. A large spillover probability introduces additional fake clusters which increase the complexity of the track finding and could have a negative impact on the tracking efficiency and eventually the physics performance of the experiment.

The analysis of the spillover probability starts by searching for clusters in the signal bunch crossing ( $BX2$ ), as well as in the previous ( $BX1$ ) and following ( $BX3$ ) bunch crossings. A cluster found in  $BX3$  is classified as spillover event, if a cluster at the same position ( $x$ ) is present in  $BX2$  and no cluster is found in  $BX1$ . The latter

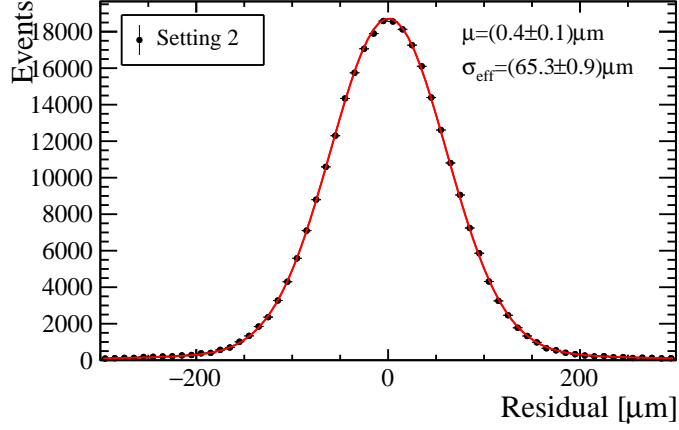


Figure 7.8: Residual distribution of the reconstructed hits. A fit of the distribution with a double gaussian is performed to determine the detector resolution.

requirement ensures that the cluster in  $BX2$  is itself not due to spillover. The spillover probability is then computed as the ratio of clusters found in  $BX3$  over the number of clusters found in  $BX2$  at the same position  $x$ .

$$P_{spillover} = \frac{N_{BX3}(x)}{N_{BX2}(x)}. \quad (7.6)$$

The measured spillover probability for both shaper settings is shown in Fig. 7.9. The channels (1151–1154) around the gap between the SiPMs have been excluded. Using Setting 1 the spillover probability is found to be about 25%. Due to the large undershoot introduced by the faster shaping of Setting 2, the spillover probability is reduced by more than a factor ten to about 2%.

Table 7.3: Average spillover probability with PACIFICr5q for shaper settings 1 and 2.

| Version | Setting | Spillover probability [%] |
|---------|---------|---------------------------|
| 5q      | 1       | $25 \pm 3$                |
| 5q      | 2       | $1.9 \pm 0.6$             |

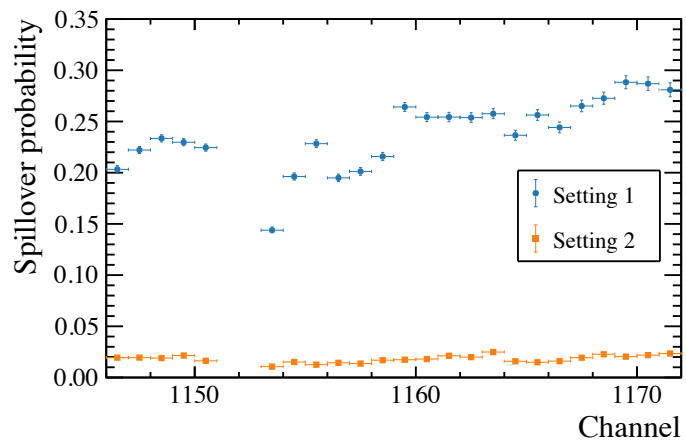


Figure 7.9: Spillover probability for shaper settings 1 and 2.



## 8 Summary

The upgrade of the LHCb detector during the LHC's Long Shutdown 2 from 2019 to 2020 will enable a major improvement in the statistical sensitivity of key observables and in the search for New Physics. To achieve this the detector will be operated at an increased instantaneous luminosity of  $\mathcal{L} \approx 2 \times 10^{33} \text{ cm}^{-2} \text{ s}^{-1}$  and read out at the LHC bunch crossing rate of 40 MHz. The new operating conditions require the replacement of the complete tracking system.

The tracking stations downstream of the magnet will be replaced by the SciFi Tracker, a large, high granular scintillating fibre tracker readout by multichannel arrays of silicon photomultipliers (SiPMs). The SiPM signals are processed by the custom designed PACIFIC ASIC, which features an analogue processing chain and three comparators for digitisation.

This thesis contributed to the development of a calibration procedure for the PACIFIC comparator thresholds, as well as to studies of the performance of the SciFi Tracker.

The calibration of the comparator thresholds relies on recording the SiPM pulse height spectrum under pulsed illumination by means of a threshold scan. A calibration procedure based on an analytical description of the pulse height spectrum has been presented and implemented into a software tool. The reliability of the calibration was evaluated and a failure rate of about 1% has been achieved. In the scope of the full SciFi Tracker 1% equates to more than 5000 channels, that are either inefficient or inactive due to a failed calibration. Further studies of the calibration algorithms are necessary to improve the reliability.

Additionally three requirements have been identified which ensure a successful calibration: the two integrators of one PACIFIC channel need to be trimmed to the same DC baseline, the delay between the calibration light pulses needs to be adjusted such that it maximise the signal amplitude, and the intensity of the calibration pulses needs to be adjusted such that it does not change the operation conditions of the ASIC.

Further studies have shown that the calibration light intensity is affected by an issue in the production of the fibre mats. A solution has been investigated to increase the intensity by increasing the duration of the voltage pulses provided to the VCSEL. The intensity was measured for several pulse widths and was found to increase by 0.09 pe/ns and 0.14 pe/ns for widths up to 20 ns and beyond, respectively. The measurement has so far only been carried out for a single VCSEL and further studies are required in order to characterise the effect for a larger sample of laser diodes.

The test beam campaign carried out in July 2018 marks the first full system test of the SciFi Tracker, where a complete slice of the detector consisting of two full width half length modules equipped with 16 SiPMs each, and readout by the full chain of frontend electronics was successfully operated. The studies presented in this thesis provide the closest measurement of the performance of the final LHCb SciFi Tracker. With the thresholds set to  $neighbour = 1.5$  pe,  $seed = 2.5$  pe, and  $high = 4.5$  pe, a hit efficiency of 99% and a hit resolution of  $65 \mu\text{m}$  has been achieved.

In addition the effect of two shaper settings has been studied. It has been shown that a faster shaping significantly reduces the fake cluster rate due to spillover. However, at the same time it also reduces the size of the integration window, making the performance of detector more sensitive to the arrival time of the signals. It is not possible to conclude which setting is ideal based on the presented results, and a dedicated study to optimise the trade-off between a low fake cluster rate and a uniform performance has to be performed.

The studies carried out in the course of this thesis verify that the detector meets the required performance and provide further input towards a successful operation of the LHCb SciFi Tracker.

# Bibliography

- [1] S. L. Glashow, *Partial-symmetries of weak interactions*, Nuclear Physics **22** (1961) 579 .
- [2] A. Salam and J. C. Ward, *Electromagnetic and weak interactions*, Physics Letters **13** (1964) 168 .
- [3] S. Weinberg, *A model of leptons*, Phys. Rev. Lett. **19** (1967) 1264.
- [4] G. Aad *et al.*, *Observation of a new particle in the search for the standard model higgs boson with the atlas detector at the lhc*, Physics Letters B **716** (2012) 1 .
- [5] S. Chatrchyan *et al.*, *Observation of a new boson at a mass of 125 gev with the cms experiment at the lhc*, Physics Letters B **716** (2012) 30 .
- [6] G. Bertone, D. Hooper, and J. Silk, *Particle dark matter: evidence, candidates and constraints*, Physics Reports **405** (2005) 279 .
- [7] T. Kajita, *Discovery of Atmospheric Neutrino Oscillations*. Accessed 13 Feb 2019.
- [8] A. B. McDonald, *The Sudbury Neutrino Observatory: Observation of Flavor Change for Solar Neutrinos*. Accessed 13 Feb 2019.
- [9] A. D. Sakharov, *Violation of CP in variance, casymmetry, and baryon asymmetry of the universe*, Soviet Physics Uspekhi **34** (1991) 392.
- [10] LHCb collaboration, R. Aaij *et al.*, *LHCb detector performance*, Int. J. Mod. Phys. **A30** (2015) 1530022, arXiv:1412.6352.
- [11] T. Gerson, *Updated sensitivity projections for the LHCb Upgrade*, Tech. Rep. LHCb-PUB-2013-015. CERN-LHCb-PUB-2013-015, CERN, Geneva, Sep, 2013.
- [12] LHCb collaboration, *LHCb Tracker Upgrade Technical Design Report*, CERN-LHCC-2014-001.
- [13] M. Thomson, *Modern Particle Physics*, Cambridge University Press, 2013.
- [14] M. E. Peskin and D. V. Schroeder, *An Introduction to Quantum Field Theory*, Advanced book classics, Avalon Publishing, 1995.
- [15] F. Englert and R. Brout, *Broken symmetry and the mass of gauge vector mesons*, Phys. Rev. Lett. **13** (1964) 321.

- [16] P. W. Higgs, *Broken symmetries and the masses of gauge bosons*, Phys. Rev. Lett. **13** (1964) 508.
- [17] Particle Data Group, M. Tanabashi *et al.*, *Review of particle physics*, Phys. Rev. **D98** (2018) 030001.
- [18] LHCb collaboration, A. A. Alves Jr. *et al.*, *The LHCb detector at the LHC*, JINST **3** (2008) S08005.
- [19] LHCb collaboration, *LHCb Operations Plot WebPage*. Accessed 16 Dec 2018.
- [20] LHCb collaboration, *Tracking and Alignment Plots for Conferences*, 2018. Accessed 18 Dec 2018.
- [21] H. Kolanoski and N. Wermes, *Teilchendetektoren, Grundlagen und Anwendungen*, vol. 1, Springer Spektrum, 2016.
- [22] Löchner, S and Schmelling, M, *The Beetle Reference Manual - chip version 1.3, 1.4 and 1.5*, Tech. Rep. LHCb-2005-105. CERN-LHCb-2005-105, CERN, Geneva, Nov, 2006.
- [23] R. Aaij *et al.*, *Performance of the LHCb Vertex Locator*, JINST **9** (2014) P09007, arXiv:1405.7808.
- [24] R. Arink *et al.*, *Performance of the LHCb Outer Tracker*, JINST **9** (2014) P01002, arXiv:1311.3893.
- [25] P. d'Argent *et al.*, *Improved performance of the LHCb Outer Tracker in LHC Run 2*, JINST **9** (2017) P11016, arXiv:1708.00819.
- [26] J. B. Birks, *The Theory and Practice of Scintillation Counting*, Pergamon, 1964.
- [27] LHCb collaboration, *LHCb calorimeters: Technical Design Report*, CERN-LHCC-2000-036.
- [28] G. Charpak *et al.*, *The use of multiwire proportional counters to select and localize charged particles*, Nuclear Instruments and Methods **62** (1968) 262 .
- [29] F. Sauli, *Gem: A new concept for electron amplification in gas detectors*, Nuclear Instruments and Methods in Physics Research Section A: Accelerators, Spectrometers, Detectors and Associated Equipment **386** (1997) 531 .
- [30] LHCb collaboration, *Letter of Intent for the LHCb Upgrade*, CERN-LHCC-2011-001.
- [31] LHCb collaboration, *LHCb VELO Upgrade Technical Design Report*, CERN-LHCC-2013-021.

- [32] LHCb collaboration, *LHCb PID Upgrade Technical Design Report*, CERN-LHCC-2013-022.
- [33] LHCb SciFi collaboration, *Material for conferences*. Accessed 10 Jan 2019.
- [34] A. B. R. Cavalcante *et al.*, *Refining and testing 12,000 km of scintillating plastic fibre for the LHCb SciFi tracker*, *Journal of Instrumentation* **13** (2018) P10025.
- [35] A. B. Rodrigues Cavalcante *et al.*, *LHCb Scintillating Fibre Tracker: Test Beam Report 2015*, Tech. Rep. LHCb-PUB-2015-025. CERN-LHCb-PUB-2015-025, CERN, Geneva, Nov, 2015.
- [36] C. Joram *et al.*, *LHCb Scintillating Fibre Tracker Engineering Design Review Report: Fibres, Mats and Modules*, Tech. Rep. LHCb-PUB-2015-008. CERN-LHCb-PUB-2015-008, CERN, Geneva, Mar, 2015.
- [37] A. Kuonen, *Development and Characterisation of Silicon Photomultiplier Multichannel Arrays for the Readout of a Large Scale Scintillating Fibre Tracker*, Aug, 2018. Presented 21 Sep 2018.
- [38] A. Ghassemi, K. Sato, and K. Kobayashi, *A technical guide to silicon photomultipliers (MPPC)*, tech. rep., Hamamatsu Photonics, K.K., Jan, 2018.
- [39] D. Renker and E. Lorenz, *Advances in solid state photon detectors*, *Journal of Instrumentation* **4** (2009) P04004.
- [40] S. Vinogradov, *Analytical models of probability distribution and excess noise factor of solid state photomultiplier signals with crosstalk*, *Nuclear Instruments and Methods in Physics Research Section A: Accelerators, Spectrometers, Detectors and Associated Equipment* **695** (2012) 247 , *New Developments in Photodetection NDIP11*.
- [41] P. C. Consul and G. C. Jain, *A generalization of the poisson distribution*, *Technometrics* **15** (1973) 791.
- [42] C. Joram and U. Uwer, *LHCb Scintillating Fibre Tracker Engineering Design Review: Frontend Electronics*, Tech. Rep. LHCb-PUB-2016-012. CERN-LHCb-PUB-2016-012, CERN, Geneva, Jun, 2016.
- [43] P. Moreira *et al.*, *The GBT Project*, in *Proceedings, Topical Workshop on Electronics for Particle Physics (TWEPP09)*, CERN, 2009. doi: 10.5170/CERN-2009-006.342.
- [44] B. Allongue *et al.*, *Custom DC-DC converters for distributing power in SLHC trackers*, in *Proceedings, Topical Workshop on Electronics for Particle Physics (TWEPP08)*, CERN, 2008. doi: 10.5170/CERN-2008-008.289.

- [45] G. Mazza *et al.*, *A radiation tolerant 5 gb/s laser driver in 130 nm CMOS technology*, Journal of Instrumentation **7** (2012) C01052.
- [46] W. Karpinski, *Light injection system performance and production*, SciFi FE Electronics PRR (2018), Accessed 28 Jan 2019.
- [47] A. Comerma and J. Mazorra, *PACIFICr5 - 64 channels SiPM readout ASIC for the SciFi Tracker detector*, 2018.
- [48] H. Chanal *et al.*, *LHCb Scintillating Fibre Tracker Engineering Design Review: PACIFIC Readout ASIC*. Geneva, Apr, 2016.
- [49] F. Alessio and R. Jacobsson, *A new readout control system for the LHCb upgrade at CERN*, Journal of Instrumentation **7** (2012) C11010.
- [50] K. Akiba *et al.*, *The timepix telescope for high performance particle tracking*, Nuclear Instruments and Methods in Physics Research Section A: Accelerators, Spectrometers, Detectors and Associated Equipment **723** (2013) 47 .

Erklärung:

Ich versichere, dass ich diese Arbeit selbstständig verfasst habe und keine anderen als die angegebenen Quellen und Hilfsmittel benutzt habe.

Heidelberg, den (Datum) .....